Summer 2012

Utilization of a tropospheric-stratospheric lidar system to study mountain induced gravity waves over jenny jump state forest

Anthony Teti
New Jersey Institute of Technology

ABSTRACT

UTILIZATION OF A TROPOSPHERIC-STRATOSPHERIC LIDAR SYSTEM TO STUDY MOUNTAIN INDUCED GRAVITY WAVES OVER JENNY JUMP STATE FOREST

by
Anthony Teti

Gravity waves are a dominant driver of the middle and lower atmospheric circulation. Yet such waves have been difficult to study due to their inherent small spatial and temporal scales and synoptic occurrence, and thus require advanced experimental systems. In this thesis first results are presented from a newly constructed tropospheric-stratospheric lidar operating at the New Jersey Institute of Technology-United Astronomy Clubs of New Jersey site in Jenny Jump State Forest in northwest New Jersey. The system utilizes a 4-W 532-nm Nd:YAG laser transmitter and a 4-inch telescope receiver to collect backscattered photons from the lower atmosphere in order to observe gravity wave structure in the troposphere and stratosphere. Advances in the optics design and receiver mount have improved the alignment and operation of the system. Relative density perturbation calculations show reflecting wave structure during the July 3, 2012 campaign above 10-km, and hint at the complexity of gravity wave reflections between the stratosphere and the ground.

UTILIZATION OF A TROPOSPHERIC-STRATOSPHERIC LIDAR SYSTEM TO STUDY MOUNTAIN INDUCED GRAVITY WAVES OVER JENNY JUMP STATE FOREST

by
Anthony Teti

A Thesis Submitted to the Faculty of
New Jersey Institute of Technology
and Rutgers, The State University of New Jersey - Newark
in Partial Fulfillment of the Requirements for the Degree of
Master of Science in Applied Physics

Federated Department of Physics

August 2012

APPROVAL PAGE

UTILIZATION OF A TROPOSPHERIC-STRATOSPHERIC LIDAR SYSTEM TO STUDY MOUNTAIN INDUCED GRAVITY WAVES OVER JENNY JUMP STATE FOREST

Anthony Teti

Dr. Andrew J. Gerrard, Thesis Advisor — Date
Professor, Department of Physics, NJIT

Dr. Dale E. Gary, Committee Member — Date
Distinguished Professor, Department of Physics, NJIT

Dr. John Federici, Committee Member — Date
Distinguished Professor, Department of Physics, NJIT

BIOGRAPHICAL SKETCH

Author: Anthony Teti

Degree: Master of Science

Date: August 2012

Undergraduate and Graduate Education:

- Master of Science in Applied Physics,
  New Jersey Institute of Technology, Newark, NJ, 2012
- Bachelor of Science in Applied Physics,
  New Jersey Institute of Technology, Newark, NJ, 2011

Major: Applied Physics

Presentations and Publications:

Teti, A. The NJIT/JJ LIDAR System and the Study of Gravity Waves: UACNJ, Jenny Jump State Forest, Hope NJ. August 2011

Teti, A. and Gerrard, A. The PENGUIn AGO program. Poster Presentation, CEDAR, Santa Fe, New Mexico. June 2011

Teti, A. The NJIT/JJ LIDAR System and the Study of Gravity Waves: NWJAA, Blairstown NJ. June 2011

Teti, A., Rodriguez, D, Federici, J, and Brisson, C."Non-Destructive Measurement of Water Diffusion in Natural Cork Enclosures Using Terahertz Spectroscopy and Imaging." Journal of Infrared, Millimeter, and Terahertz Waves April (2011): 513-27.

Teti, A. The NJIT-UACNJ-PSU Collaborative: A spatially scanning middle atmospheric lidar system in northwest New Jersey: Poster Presentation, CEDAR, Boulder, Colorado. June 2010

To my high school physics teacher, Mr. Scheneck, who introduced me to the joy and challenges in physics. Without his teachings and guidance, I may never have decided to take the route of physics. To Dr. Andrew Gerrard, who saw my potential and convinced me to stay for graduate school. I cannot thank Dr. Gerrard enough for funding my graduate schooling as well as the tons of guidance he has given me over the years. To Dr. Melville, who mentored me in electronics and machining. To Gil Jeffer, who spent countless hours, even all nighters, aiding and accompanying me during the lidar data collection process at Jenny Jump State Forest. To Kevin Urban, who spent numerous hours helping me prepare for the toughness of my future courses, and kept my spirits high during the most challenging times of graduate school. To Dhvanit Mehta, who helped me work out many of the vigorous problems electrodynamics and quantum mechanics had to offer.

Most importantly, I would like to thank my parents, whose constant support and encouragement through school made it possible for me to succeed in college. I cannot thank them enough for their love and understanding during the most challenging times of my life. To my girlfriend Katie, who has kept me happy and motivated during my graduate years.

ACKNOWLEDGMENT

I would like to thank the following for their contributions which made my thesis possible: Dr. Andrew Gerrard, my thesis advisor, who taught me how to properly research and whose expertise in atmospheric lidar made this thesis possible; Dr. John Federici, committee member, who let me as an undergraduate work in his lab, which made me choose the field of optics for my thesis; Dr. Dale Gary, committee member, who put time and effort on behalf of my thesis; Dr. Robert Melville, whose machining and electronics expertise made the lidar system fully functional; Gil Jeffer, the United Astronomy Clubs of New Jersey (UACNJ), and Jenny Jump State Forest for making this research possible; my lab mates Kevin Urban and Dhvanit Mehta; and Christine Oertel and everyone else at the Center for Solar-Terrestrial Research.

TABLE OF CONTENTS

TABLE OF CONTENTS
(Continued)

Chapter **Page**

LIST OF FIGURES

LIST OF FIGURES
(Continued)

Figure **Page**

LIST OF FIGURES
(Continued)

Figure **Page**

LIST OF FIGURES
(Continued)

Figure **Page**

CHAPTER 1

INTRODUCTION

1.1 Earth's Atmosphere

The Earth's atmosphere is divided into several regions and sub-regions based on specific characteristics that differentiate them from each other. Each region is generally defined by altitude and temperature and Figure 1.1 illustrates the different regions of the atmosphere.

The outermost region of the atmosphere, known as the exosphere, ranges from 700-1000 km away from the Earth's surface and contains very low amounts of helium, carbon dioxide, and molecular oxygen[1]. The density is so low that the atmosphere at this point does not behave like a fluid, and particles may travel several hundreds of kilometers before having a collision. The magnetosphere is an area that contains charged particles, and extends from several Earth radii to tens of Earth radii. It is the magnetosphere that blocks extremely harmful solar wind from penetrating into the Earth's atmosphere. The next region known as the thermosphere, ranges from approximately 100-700 km in altitude and is where satellites and the International Space Station orbit. The thermosphere also contains most of the ionosphere, which is a shell of electrically charged particles. The ionosphere has the ability to reflect radio waves, thus making radio communication on Earth at far distances possible. The mesosphere, from approximately 60-100 km is the primary area where meteorites burn up. This is due to the increased density in comparison to the thermosphere and exosphere which allows for ablation to occur. The second innermost region of the atmosphere is the stratosphere, ranging from approximately 15-60 km. Within the stratosphere contains the ozone layer, which blocks large amounts of harmful ultraviolet radiation. The troposphere is the lowest region of the atmosphere, ranging from the ground surface to $\sim$10 km near the poles,

[1]This is just an approximation, the exosphere does not have a well defined upper limit.

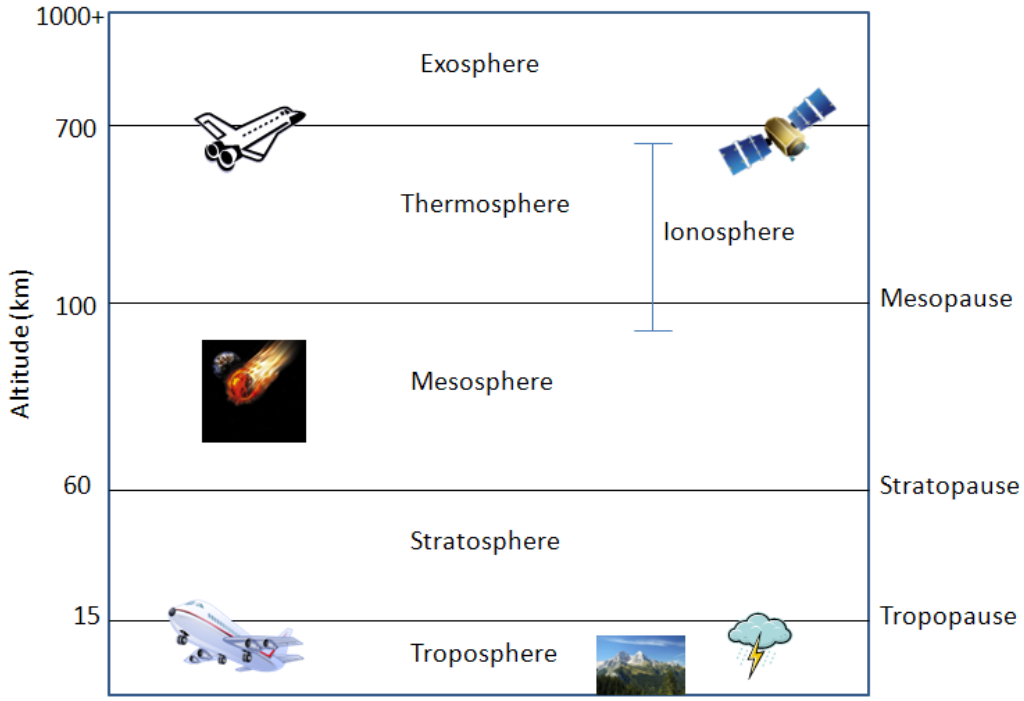

Figure 1.1 Illustration of the Earth's Atmosphere.

and up to ∼15-20 km by the equator. Weather is generated almost completely in the troposphere. Although it is the smallest of the major regions of the atmosphere, it contains 80% of the atmosphere's mass and 99% of it's water vapor [Parker et al., 1984]. With most of the atmosphere's mass and water vapor concentrated in the troposphere, instabilities occur often which can produce gravity waves.

1.2 Gravity Waves

Gravity waves, also known as buoyancy waves, are disturbances in a fluid that are associated with gravity as the primary restoring force. They are similar to waves on the ocean, except that the wave propagates through air instead of water. Atmospheric gravity waves can be created at altitudes from the ground level up through the mesosphere. Gravity waves are initiated by an impulse to the atmosphere and such generators include topological variations, convection, and wind shear. Gravity waves generated by convection involve a time-varying thermal forcing associated with latent heat release that can interact with overlying stable layers (e.g. Fritts

and Alexander et al. [2003]). These types of waves can be very complex and are not well understood. Wind shear generated gravity waves occur when wind flows against an unstable fluid layer, similar to a Kelvin-Helmholtz instability. The gravity waves created by unstable shears have been studied for numerous years and still remain one hardest to quantify [Fritts and Alexander et al., 2003]. Mountain waves, gravity waves generated from topological sources, were among the first to be studied [Gill et al., 1982]. Figure 1.2 depicts the generation of gravity waves by a topological source. These mountain waves occur when a flow, traveling in a horizontal direction, is deflected over a large mass.

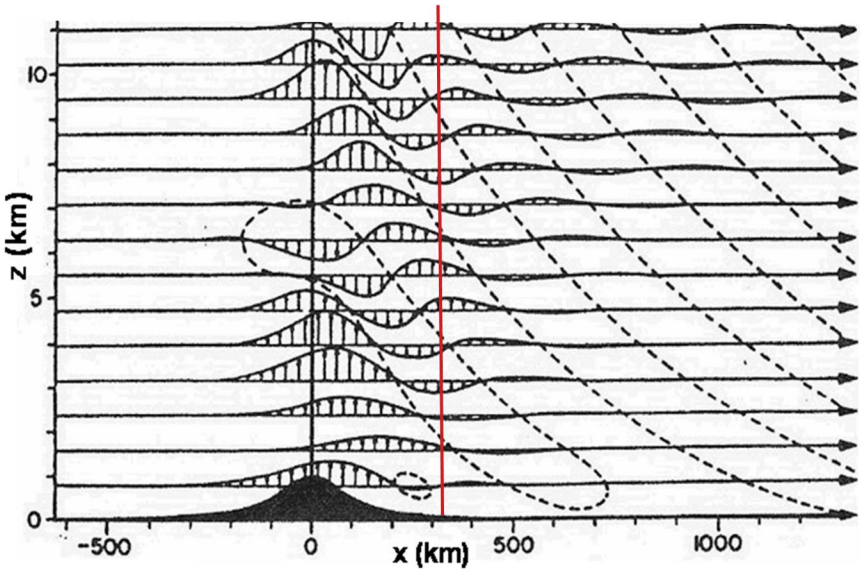

Figure 1.2 Graphical Representation of Mountain Induced Gravity Waves. [Salby et al., 1996]

The air has no other direction to flow besides upward, pushing up underneath the existing air mass. This upward motion of the flow continues until the mass becomes much denser than the surrounding layer. The air mass then falls back down because it is denser than its surrounding environment; this starts the oscillation which creates the gravity waves shown in the figure. These waves can continually propagate for many hours, and can travel for many hundreds of kilometers, as depicted in Figure 1.2. Mountain waves, generated within the troposphere at low

altitudes, can continue to propagate upward from the lower atmosphere into the middle atmosphere. At 10-110 km altitudes, these waves can increase greatly in amplitude due to the decrease in density, and affect atmospheric circulation, structure, and variability on a large scale of tens to a hundred kilometers [Fritts and Alexamder et al., 2003].

First recorded observations of gravity waves began in the early 1800's in response to a phenomenon that occurred to the west side of the Pennine mountains in England [Gill et al., 1982]. Known as the Helm wind, early accounts indicated that these furious winds were strong enough to "break trees, overthrow stacks of grain, and throw a person from his horse." Studies of mountain induced gravity waves began in the 1920's-30's using balloons and gliders [Gill et al., 1982]. Theoretical calculations of this wave phenomenon did not occur until the mid-1940's. In particular, Lyra et al. 1943 found solutions for a flow over rectangular shaped mountains. In 1948, Queney found solutions for flow over a mountain that had a "bell-shaped" ridge. Modern mathematical techniques can find solutions to these waves over various shaped surfaces in both two and three-dimensions.

Today it is known that gravity waves, mountain waves in particular, result in clear air turbulence that can be very dangerous to aircraft [Dutton et al., 1970; McCann et al., 2001]. It is possible that gravity waves can control the location and timing of significant weather events [Nappo et al., 2002], including tornado formation [Coleman et al., 2008]. The coupling mechanism of lower atmospheric gravity waves with the middle atmosphere, and the resultant effect is still not fully understood. Modern advances in technology have allowed for *in situ* rockets, satellite and remote sensing techniques, such as lidar, to study these waves in more detail.

1.3 Lidar

Light identification, detection, and ranging (LIDAR, or lidar), is a modern optical remote sensing technique that measures scattering properties of distant objects. Modern Lidar based techniques have been around for more than forty years, though there has been a recent increase in popularity due to its wide variety of applications and potential. Today lidar applications are used in the fields of advanced atmospheric studies, geology, soil science, military, law enforcement, and topography. Lidar techniques came into existence in the late 1930s as a way to measure properties of the atmosphere. These primitive systems pioneered by Hulburt in 1937, used searchlights beams to measure aerosol layers [Hulburt et al., 1937]. His system's accuracy limited measurement range to a maximum of 10 km, less than 5% of the total atmosphere. The advent of modern lidar systems begin with the invention of the laser. The ruby laser, developed in 1960 [Maiman et al.,1960], was immediately implemented in lidar systems and first began measuring high altitude clouds [Collis et al., 1965]. Limitations in resolution and accuracy of the data were due to poor pulsing techniques. For decades a mechanical chopper was used that would allow the laser to pulse at a rate of up to tens of hertz. The Q-switch, first proposed by Gordon Gould in 1958 [Taylor et al., 2000], and developed shortly after the invention of the laser, greatly improved and replaced the role of a mechanical chopper on lidar systems. The Q-switch is an attenuating device attached to the laser to produce a pulsed output instead of a continuous beam. Q-switching allows for pulsing of tens of thousands of hertz, values that are nearly impossible to reproduce with a mechanical chopper. Faster and more reliable pulsing allows scientists increased resolution and shorter bin width durations. The atmospheric lidar community, in particular, has followed the advancements in laser technology. Beginning from the mid-1960's lidar has evolved from the original ruby lasers to CO2, helium neon, and solid state lasers. Today, the most powerful and reliable lasers are the Nd:YAG

solid state lasers, and have been used in lidar for the last decade [Koroshetz et al., 2005]. Use of a ground based remote sensing technique such as lidar is one of the most cost effective ways to obtain atmospheric temperature, density, and composition measurements. Figure 1.3 shows an example of the lidar using a 532nm laser to take atmospheric density measurements at Jenny Jump state forest. The United Astronomy Clubs of New Jersey (UACNJ) observatory at Jenny Jump is a relatively dark-sky location atop a sharp ridge at an elevation 300+ meters above sea level in Hope NJ [NJDEP et al., 2012]. It is believed that this northwest-southwest oriented ridge, the Kittatinny mountain ridge, located approximately 25km to the west, and other similarly oriented ranges along the Appalachian trail are strong generators for gravity waves. In addition, the Appalachian mountains, only tens of kilometers to the west, may be even a stronger generator of mountain gravity waves. Figure 1.4 shows the location of the field site, and illustrates the possibilities of mountain wave paths and activities. The lidar system, using a 4W 532 nm Nd:YAG laser and 4 inch telescope, will take temperature and density measurements in search of gravity wave activity in the troposphere over Jenny Jump State Forest. If gravity waves are observed, characteristics of the wave such as period, wavelength, and duration of the wave will be found from the data collected. In addition, ray tracing methods will be used to determine the source location of these mountain gravity waves over Jenny Jump State Forest.

Figure 1.3 NJIT Lidar System Operating at Jenny Jump State Forest. Image Taken by Chris Callie.

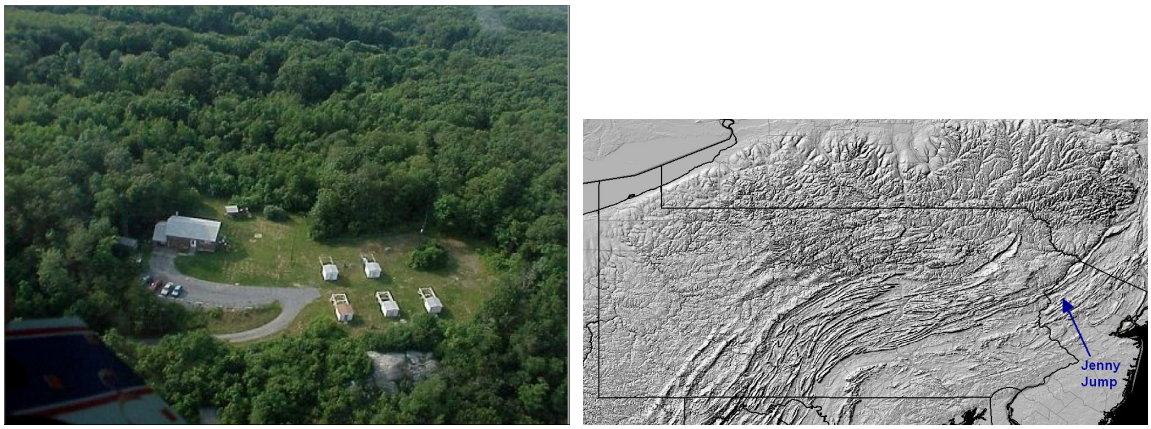

(a) **(b)**

Figure 1.4 Image (a) is an Aerial View of UACNJ Obsevatories at Junny Jump State Forest. Illustration (b) Shows the Topology of the Area Surrounding Jenny Jump State Forest (USGS National Map Seamless Server Viewer).

CHAPTER 2

THE LIDAR FORWARD MODEL

A forward model is an essential aid in fully understanding the experiment. A forward model encompasses many of the optical and instrumental considerations in the experiment to try an estimate what the experimental data will predict. Considerations such as atmospheric density per altitude, laser power, and background noise are only a few parameters needed for an accurate lidar forward model. A complete set of atmospheric, instrumentation, and optical parameters will allow one to approximate the number of photons backscattered by a lidar system per given height. After all these parameters are combined, the result become known as the lidar equation.

2.1 Lidar Equation

The lidar equation is given by [Gardner et al., 1989]:

$$N(z) = (\eta T_A^2)(\frac{P_L \tau}{\frac{hc}{\lambda}})(\sigma_{eff} n_s(z) \Delta z)(\frac{A_R}{4\pi z^2}) + N_B R \tau \tag{2.1}$$

Where:

η = lidar system efficiency

T_A^2 = transmittance of the lower atmosphere (%)

P_L = laser's power (W)

τ = integration time (s)

h = plank's constant (J·s)

c = speed of light (m/s)

λ = laser's wavelength (m)

σ_{eff} = effective molecular backscatter cross section (m^2)

$n_s(z)$ = molecular density at range z (m^{-3})

Δz = receiver range bin length (m)

A_R = receiving telescope aperture area (m^2)

z = altitude (m)

N_B = Expected number of photons due to background noise and dark counts

R = Laser pulse rate (Hz)

The first variable in the equation η takes into account each of the optical efficiencies in the lidar system. It can be determined by multiplying all of the optical efficiencies. η is given by: η = Efficiency of the Telescope $\times$ Lens $\times$ Filter $\times$ PMT Quantum Efficiency. Plugging in the respective values for a typical system gives:

$$\eta = 0.8 \times 0.8 \times 0.5 \times 0.15 = 4.8\% \tag{2.2}$$

It is enough to state the T_A parameter as transmission of the lower atmosphere (less than 40km) because the transmission will greatly decrease as the altitude increases. The transmittance of the lower atmosphere as provided by Andrew Gerrard (unpublished values, 2012) can then be approximated to be:

$$T_A^2 = 82.5\% \times 82.5\% = 68\% \tag{2.3}$$

The laser can have a power of between 3.5-4.5 W depending on tuning, and a value of 4W will be used in this forward model. An integration time τ of 30 seconds was chosen. This time is chosen to sufficiently collect enough photons per bin, but not long enough to reduce temporal resolution.

The effective molecular backscatter cross section σ_{eff} , converted to units of (m^2) is given by [Measures et al., 1984]:

$$\sigma_{eff} = 5.45[\frac{550}{\lambda(nm)}]^4 \times 10^{-28}\text{cm}^2 = 6.226 \times 10^{-32}\text{m}^2 \tag{2.4}$$

which describes the area that each molecule will Rayleigh scatter radiation downward.

The molecular density N_s at range $z(cm^{-3})$ was obtained from Brasseur et al.1986. This parameter takes into account the density of the air at altitude z and helps in determining the amount of backscatter to be observed based on the amount of molecules at z.

The receiver range bin length Δz can be calculated to be:

$$\Delta z = \frac{c\Delta t}{2} = 48\text{m} \tag{2.5}$$

where Δz is the distance the laser light pulse has traveled in Δt seconds. This is an important calculation to determine the SR430 bin width, which will be discussed in Chapter 3. The receiver telescope aperture area A_R can be calculated to be

$$A_R = \pi r^2 \tag{2.6}$$

where r represents the radius of the primary mirror. However, reduction of the overall aperture area by the secondary mirror can be considered and calculated by:

$$A_R = \pi(r_{primary})^2 - \pi(r_{secondary})^2 \tag{2.7}$$

This calculation yields a reduction of the aperture area from 0.0087 m^2 to 0.0079 m^2. This small difference in aperture area reduces the total expected number of photons by 10%, which is significant. Therefore the secondary mirror needs to be accounted for in all calculations. The altitude z will be used in the forward model at increments of 5km, which matches molecular density N_s reference data. Interpolation will be used to obtain an expected number of return counts at increments of 1km. The remaining constants N_B , R, and τ added to the equation takes into account the expected number of photons due to noise. N_B, the noise due to dark counts, is a value that is found during background measurements taken while the laser is off. This measurement specifies system noise and electromagnetic interference from the

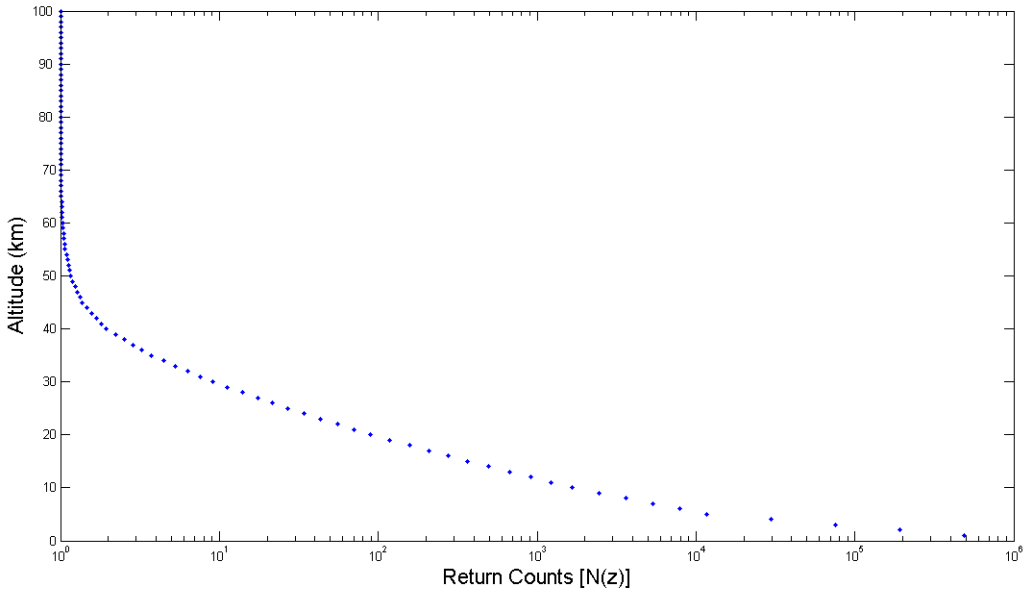

Figure 2.1 Expected Number of Backscattered Photons per Altitude Using a 4W 532nm Laser.

close proximity of all the components. The laser pulse rate R, and integration time τ are multiplied against background noise by dark counts to account for the total duration of the measurement period. For modeling purposes an $N_B R\tau$ of 1 will be used, since at least 1 count needs to be in each bin in order for background subtraction to occur. Inserting all the parameters into the lidar equation gives $N(z)$, the number of photons measured per unit time and altitude range.

Figure 2.1 shows the expected return counts N(z) at altitude ranges of 1-100km at 1km intervals. At 5km the expected photon return counts is approximately 1.18×10^4 compared to 4 at 35km (which approaches the background number of return counts). At an altitude of 5km, 96% of all expected backscattered photons have been collected. By the altitude of 35km, 99% of the expected number of photons have been collected. As the altitude increases, the amount of return counts collected significantly decreases, as shown in the figure above. This low amount of backscatter at higher altitudes is primarily a result of the significant decrease in atmospheric density. Another important factor is the z^2 altitude term in the lidar

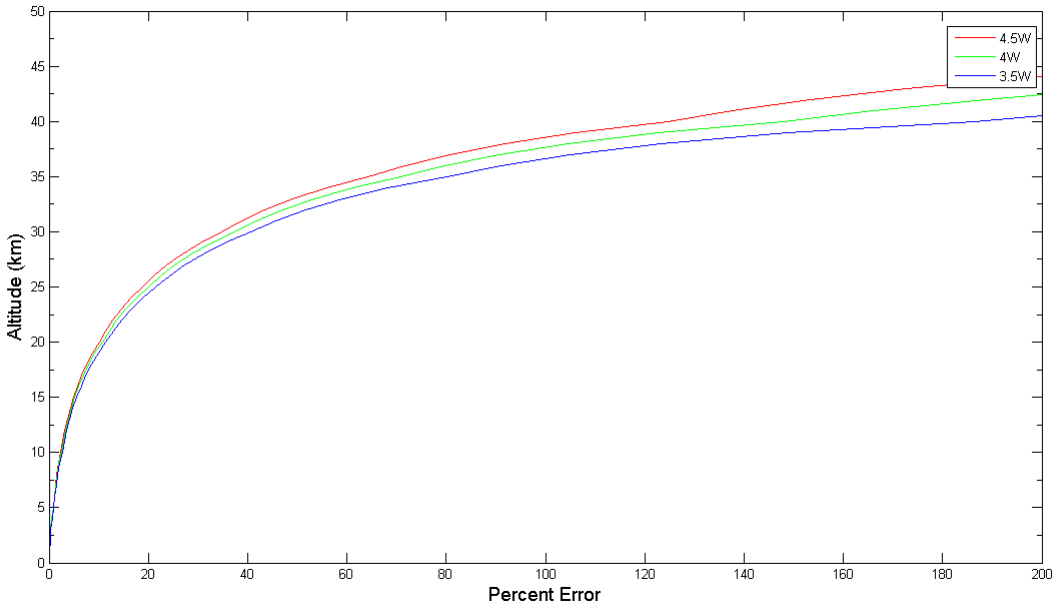

Figure 2.2 Lidar Percent Error for Multiple Laser Powers.

equation. As the altitude increases, the $1/z^2$ term behaves as an inverse square relation, greatly reducing the number of counts.

2.2 Percent Error

The lidar equation aids in understanding how the lidar system will function and forecasting the outcome of experimental data. It is also important however to understand the importance of percent error in this approximation. The error can be calculated by using the equation :

$$PercentError = \frac{\sqrt{N_z}}{N_z - N_B} \times 100 \tag{2.8}$$

in which the number of photon counts received (N_z) is divided by the difference between the photon counts received (N_z) and the expected background noise (N_B).

Figure 2.2 depicts the percent error for different laser powers. Therefore, by using a 4W 532nm laser, one can expect the estimated return counts per altitude er-

ror to be 100% below 35km. For most applications this error seems extremely high, but for lidar this is fine, as it can be used to determine the expected trend/profile of the experimental data. In addition, high percent error allows ways of improving the accuracy of the system. Different laser powers affect the accuracy in the measurements as shown in the graph. An increased laser power provides a larger number of photons that can be backscattered and collected, improving the accuracy of the measurements by increasing the signal to noise ratio. By increasing the laser power from 3.5W to 4.5W, the lidar's percent error decreases by several percent at low altitudes, and tens of percent at higher altitudes. This plot can also be used to determine the cutoff altitude, i.e. the altitude that allows for a reasonably low percent error. The current tropospheric-stratospheric lidar system configuration allows for measurements up to approximately 25km.

There are several ways to improve accuracy in measurements and reduce percent error. One of the main techniques practiced by the lidar community is to increase laser power. As shown by the figure above, increasing the power of the laser will increase the amount of backscattered photons which improves accuracy (and directly lowers error). By replacing the current NJIT lidar laser with a 8W 532nm laser and using the current 4inch telescope, the percent error decreases by half at 35km (assuming the original laser has a power of 4W).

In addition to to improving the laser, another practical approach is to increase the size of the telescope. Having a telescope with a larger primary mirror will allow the system to collect more photons. Collecting more photons per unit time will increase the signal to noise ratio and provide more accurate results. Therefore another consideration in improving the lidar system would be to upgrade to a larger telescope. If the 4inch telescope were to be replaced with a 48inch while utilizing the current laser, the percent error would be reduced significantly, as shown in Figure 2.3.

With a 48inch telescope, the error would drop significantly to 2% or less at

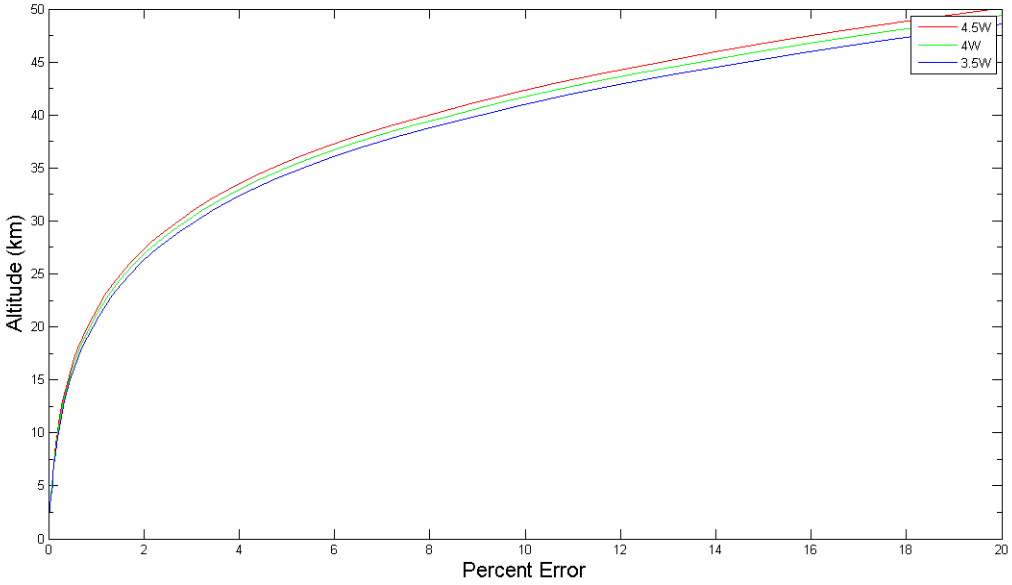

Figure 2.3 Lidar Percent Error with 48inch Telescope for Multiple Laser Powers.

25km. If both a higher powered laser and a larger telescope would replace the old system, then the error would be much lower, at a fraction of a percent. It is also important to understand that improving components also improves the maximum altitude of measurements that can be taken. If the new larger telescope were implemented into the system, and a laser power of 4W, then measurements would able to be taken up to 50km with less than 20% error, the same as the current systems error at 20km. Improving the transmitting and receiving components is how the lidar community can now measure up into the upper stratosphere and mesosphere with great accuracy. However, in the case of studying tropospheric and lower stratospheric phenomenon, a cost effective smaller system is sufficient.

CHAPTER 3

INSTRUMENTATION

Understanding the instrumentation in a lidar system is crucial to understanding how data is acquired. Also, having knowledge of the individual components and their functions will allow for proper diagnosis and replacement of individual system components possible. The tropo-strato lidar system is composed of transmitter, receiver, and data acquisition components.

3.1 Transmitter Components

The main transmitter components consist of a laser and pulse/function generator. The neodymium YAG laser is a type of solid state laser and is used in the tropo-strato lidar system. Its lasing material is a combination of neodymium, used as the dopant, and yttrium, aluminum and garnet that are used in making the crystal medium. Its Q-switching design allows it to pulse at 10Hz with a pulse duration of 5 nano-seconds. It produces a 1064 nm infrared beam at 9W. In order for the laser to emit radiation in other wavelengths, harmonic crystals are used. Figure 3.1 displays the laser with two additional sections that contain the harmonic crystals.

The first harmonic crystal converts the incident infrared light into a green visible beam at 532nm. From this transition through the crystal, power decreases to 4W. Another harmonic crystal is then used to drop the radiation to ultraviolet at 355nm. The power again decreases to 2W. Tuning the harmonic crystals allows for power adjustment at both the 532nm and 355nm wavelengths. It is important to note that both crystals can not be individually optimized to achieve maximum power out of the third harmonic. It is necessary to tune both crystals since the harmonic oscillators in combination do not respond to tuning linearly. Experimental tuning between crystals with frequent power measurements is the only method to achieve maximize power. Figure 3.2 shows an image and schematic of the interior of the

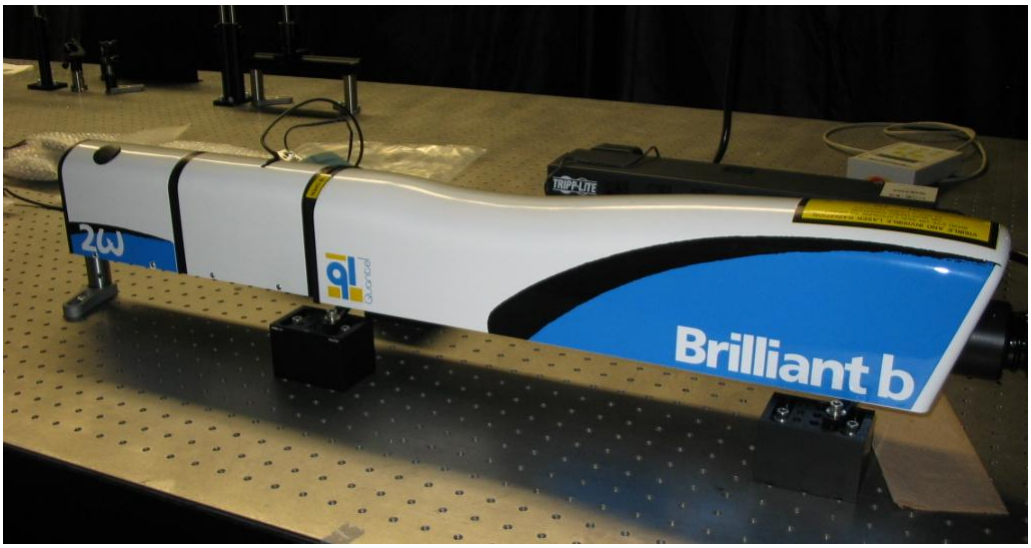

Figure 3.1 Laser Including both Harmonic Crystals. Image Credit: Salman Naqvi.

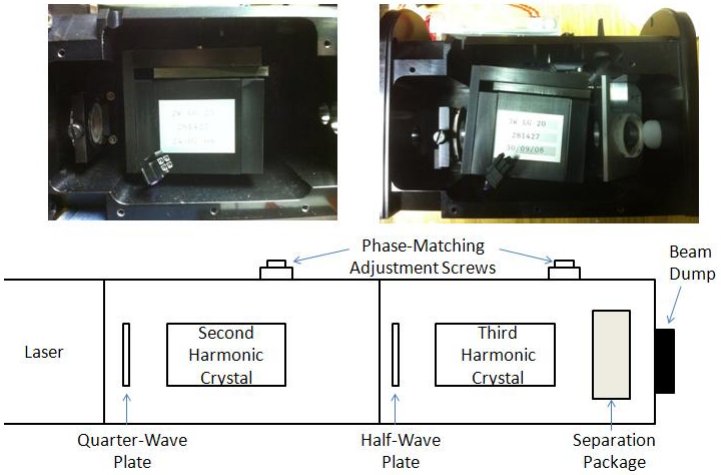

Figure 3.2 Schematic of the Harmonic Oscillators.

second and third harmonic oscillators.

The laser is water cooled to 37°C to ensure the harmonic crystals optical properties are held constant. The powers stated above are maximum powers measured at each wavelength. Actual power measurements will be included in the data analysis section.

Other style lasers were considered, however a solid state laser met certain required criterion. A solid state laser, unlike many dye and gas lasers, are capable of achieving high enough powers needed in atmospheric lidar applications. In addition,

the recent popularity of solid state lasers has increased within the science and commercial industry considerably. This increasing demand of infrared lasers have made manufacturing competitive and solid state lasers a cost effective choice. Therefore choosing a laser in the infrared spectrum and attaching harmonic crystals to change the its wavelength provided the lidar system with a wider range of available powers and frequencies to pulse into the atmosphere.

3.2 Receiving Components

The lidar system's receiving components include a photomultiplier tube, high voltage power supply, preamplifier, and an optics tube. Discussion of the telescope will be included in the field of view section.

Since the photomultiplier tube (PMT) is very sensitive in the ultraviolet, visible, and near infrared spectrum, it makes for an ideal detector for lidar applications. The PMT's main objective is to count photons. A voltage drop observed by the PMT corresponds to an incident photon on the PMT's detector. A cooler is connected to the PMT to reduce the number of thermal dark counts. A high voltage power supply provides the necessary 1500 volts to the photomultiplier tube. The Stanford Research SR445A signal preamplifier is connected to the PMT and provides an overall gain of 5x (at 50Ω). This amplifies the output voltage from the photomultiplier tube to a suitable level that can be read by the SR430 and oscilloscope. The lenses and filters provide a 532 nm collimated beam by blocking all other frequencies. A general optical layout of the receiver optics tube, Figure 3.3, is shown below. Knowing the layout of the optics tube can help in determining the specific lens and filters needed. Several limiting factors, including size of the optical bench, focus of the telescope, optical tube sizes, and availability of lenses led to the specific design of the optical tube. The specifics of the optical tube are shown in figure 3.4.

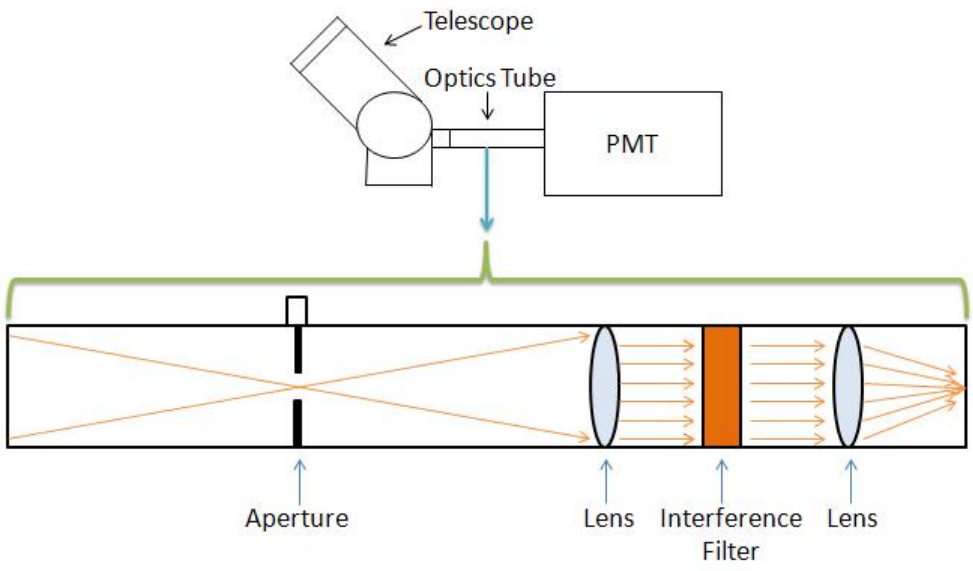

Figure 3.3 Receiver Optics Tube.

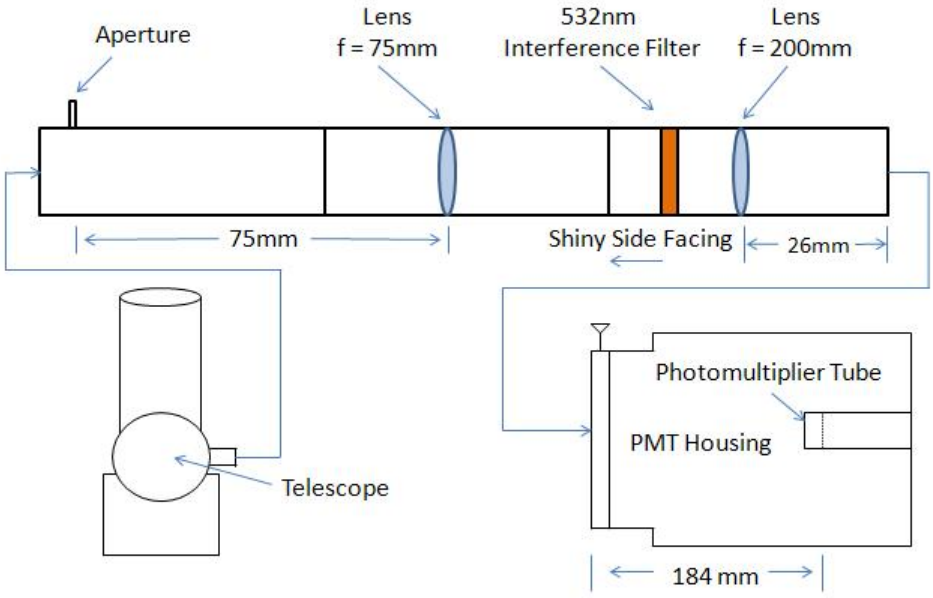

Figure 3.4 Optical Design Schematic.

Incident light is focused by the telescope, whose focal point is set on the aperture. The first lens collimates the beam as it passes through the optics tube and toward the interference filter. The interference filter allows only 532 nm light to pass, and the second lens focuses the collimated beam on the detector of the photomultiplier tube.

3.3 Data Acquisition Components

Data acquisition components in the system include an oscilloscope, SR430 multichannel scaler and averager, and a computer. An oscilloscope is used primarily to check the voltages that are output from the preamplifier. The oscilloscope will allow the user to visually inspect for any irregularities and noise in the signal. Also, the oscilloscope is used to measure voltages and waves produced by the function generator, for dark count measurements. The SR430 multichannel scaler/averager counts incoming pulses in successive time bins. The duration of the time bins can be set between 5ns and 10.5ms [Stanford Research Systems et al., 2007]. Since the laser pulse duration is 5ns, a bin time duration should be longer but well before the time before the next pulse is sent. The equation:

$$\Delta r = \frac{c\Delta t}{2} \tag{3.1}$$

refers to the receiver range bin calculation. This calculation allows the user to determine the spatial range or time measurements with reference to the speed of light. This explains the phenomenon that laser light traveling at c will travel from an origin, backscatter off a molecule, and return to the origin in time Δt, and is the same as term Δz from the lidar equation. An illustration of receiver range binning is shown in Figure 3.5.

If a Δt of 0.32 μs is chosen, then by the above equation, the range bin Δr can be calculated to 48 meters. Therefore each bin will essentially have a number of collected photons pertaining to every 48 meters of the atmosphere. Using all 1024 bins will allow a total range of measurements of $\sim$49 km. Depending on the altitude that the mountain induced gravity waves are measured, changing Δt which would directly change Δr and could provide more accurate resolution. If mountain induced gravity waves are only measured to 20km (at Jenny Jump) then there is

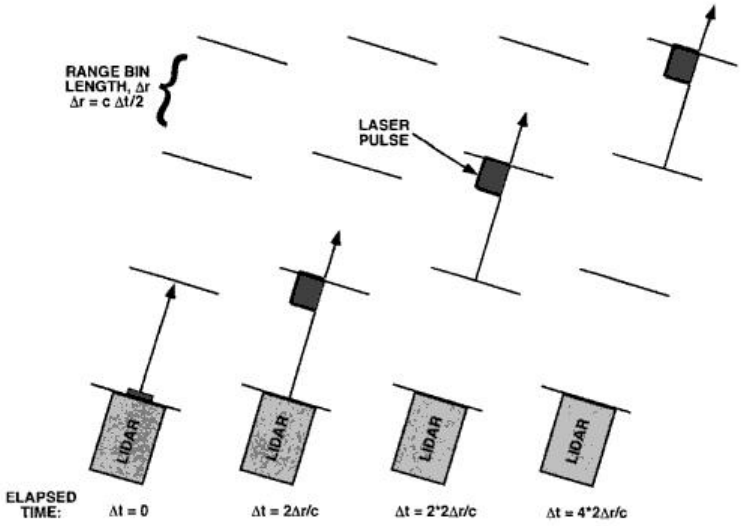

Figure 3.5 Graphical Representation of Receiver Range Binning [Driggers et al., 2003].

no need to measure a full range of 49 km. Performing a few simple calculations would determine a $\Delta t = 0.13$ μs and $\Delta r = 20$m. This new result would allow for twice the resolution as the earlier example. It is important to note that bins corresponding to high altitudes need to be reserved for background subtraction. If N is the number of bins, then $\sqrt{N}$ need to be reserved for background counts. For an SR430 using 1024 bins, at least the last 32 bins should be reserved for background noise. Therefore for the above example of $\Delta r = 48$m, it it is assumed that at an altitude of 47.5-49km will be counts of all background, and not backscatter of the lidar. This concept is essential for background subtraction. Without it, one will not be able to distinguish between background/system noise, and photons scattering off the atmosphere from the lidar. Incorporating this concept is also necessary to to eliminate photons observed from the moon. To ensure background counts are properly subtracted, a receiver range bin length of 320 nanoseconds is used. The integration time, the time in which the SR430 collects data until it repeats, is set to 30 seconds. How the SR430 collects and displays the data is illustrated in Figure 3.6.

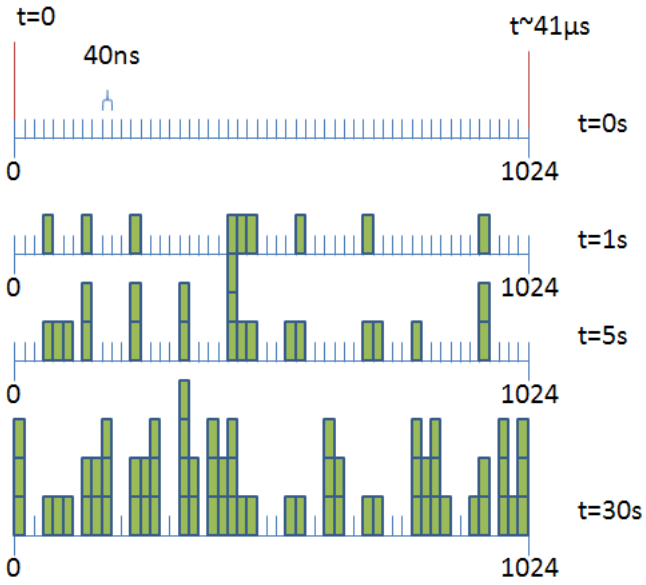

Figure 3.6 Illustration of How the SR430 Collects Photons. Each Photon Counted Will be Tallied in it's Corresponding Bin.

At $t = 0$ there are no counts, as expected, since the SR430 has not been triggered by the laser yet. The laser then pulses, immediately triggering the SR430 to start counting. As described above, each bin corresponds to a time and altitude range. For an integration time of 30 seconds, the SR430 will continually collect photons and tally them in their corresponding bins. After 30 seconds, the SR430 will send the data to the computer and clear all the bins and begin counting again. This cycle repeats for the total operation time set by the user.

The software used by the lidar system is a LabVIEW script written by students at Pennsylvania State University. The code communicates to the SR430 via a general purpose interface bus (GPIB) connector and controls the trigger level, trigger slope, discriminator level, discriminator slope, and collection duration time. The trigger level is a voltage set, and only when this value is met the SR430 will begin counting. The discriminator level is set to a level above the cable and system noise to ensure the count is a real photon. The trigger and discriminator slopes can be set to either positive or negative to determine which part of the signal should be considered and counted. The front panel of the software is shown in figure 3.7.

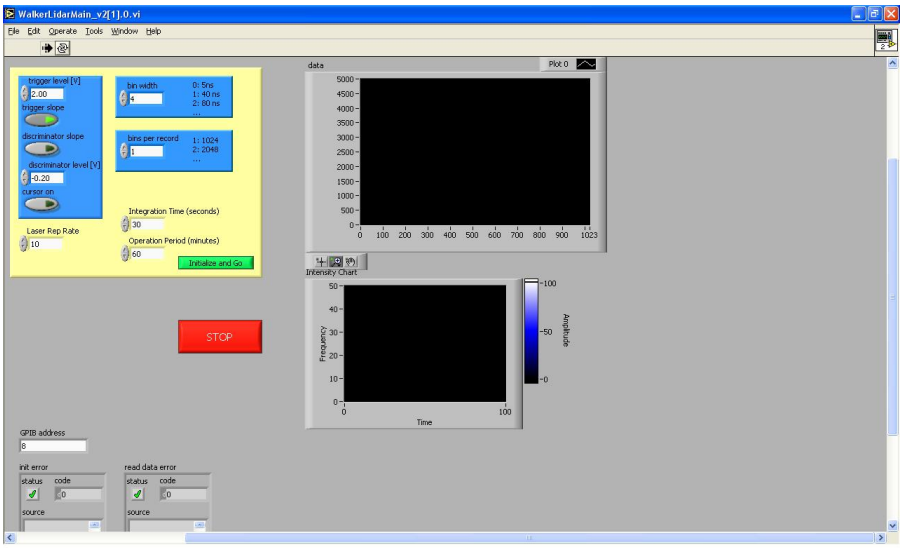

Figure 3.7 Labview Front Panel That Controls the Lidar System.

Preset bin width options and bins per record are also allowed to be chosen through this GUI program. This program grants the operator the ability to change parameters on multiple instruments on a computer. This allows for fast setup and changes while taking measurements. The program displays the SR430 data and the frequency vs. time data during measurements. When the system has completed data collection, the software writes the collected data to an ASCII text file. The first column of the file contains the time stamp of when the data collection has started. Columns correspond to bins 2 through N+1 and contain the number of photons collected during a specific integration time. For an integration time of 30 seconds, operation time of 60 minutes, and 1024 bins, the data will be written as a 120x1025 matrix. This corresponds to 120-30 second intervals in the 60 minutes of runtime, the first column the time stamp of data collection, and the amount of photons collected in bins 2-1025.

Dark count measurement can be taken to ensure the data is real and not an artifact of system noise. This can be done indoors by running the system using a function generator to pulse the system instead of the laser. With the shutter closed and the program running, the system noise can be observed and collected.

3.4 Sequence and Schematic of Components

A schematic of the system is shown in Figure 3.8. Arrows on the schematic indicate

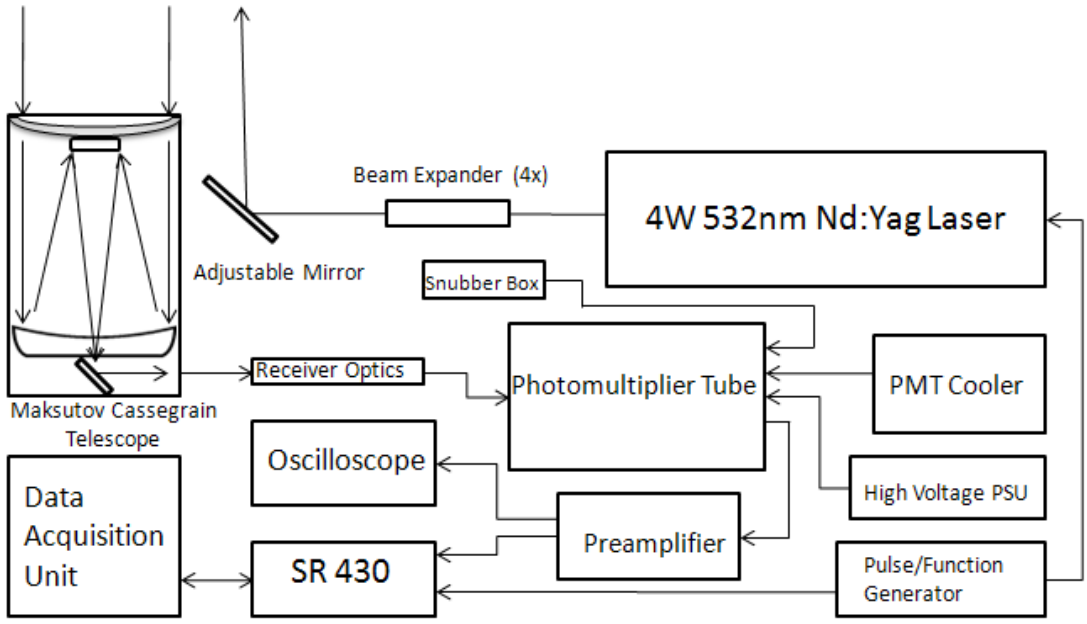

Figure 3.8 Schematic of the Tropospheric-Stratospheric Lidar System.

the corresponding path of the light and signal and can be reiterated in words as the following. With the Q-switch activated, the laser pulses at 10Hz with a 5ns beam duration, which passes through a 4x beam expander. The 8mm beam expands to 32mm and reflects upward off a mirror. Photographs of the 4x beam expander are shown in Figure 3.9.

Each of the 5ns pulses have a probability of causing the molecules in the beams path to oscillate at its ground state. The oscillating molecule then may emit radiation, which is collected by the telescope. The telescope begins focusing the light, and the filters and lenses allow only the collected light at a 355nm to enter the photomultiplier tube. The photomultiplier tube, which is cooled and powered by the high voltage power supply unit and cooler, takes the incident photons in which a voltage conversion is performed. The voltage is increased by 5 from the

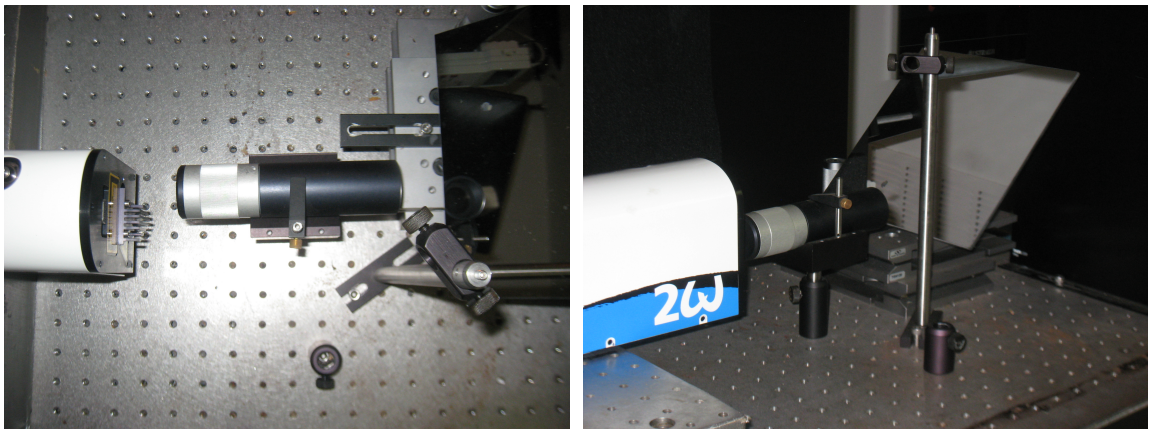

(a) (b)

Figure 3.9 4x Beam Expander. Photos Taken By Gil Jeffer.

preamplifier and the signal is sent to the SR430 multichannel scaler and averager. The SR430 takes the signal based on the number of photons and places them in bins determined by the time of collecting. This allows the user to determine how many photons were collected at a certain time interval, which relates directly to density of the air per altitude range. After assortment of data from the SR430, it is sent to a computer. A LabVIEW script takes all the data and stores the amount of counts per bin per 30 second interval in an array.

Proper storage of the system is essential to prevent damage of the optical parts from weather. The system has been mounted onto a cart, displayed in figure 3.10. This ensures that the optics will remain properly aligned during transit. In addition, moving a cart instead of individual components prevents instrumentation from being damaged. The lidar system is stored in a building while not in use, to reduce weather related wear on the instruments.

3.5 Field-of-View

The tropo-strato lidar system uses a 0.105m (4inch) Maksutov Cassegrain Meade telescope. This telescope has a focal length of 1.47m and an f-number of 14. The specifications given above will allow for telescope field-of-view calculations. Field-

Figure 3.10 Lidar Instrumentation Mounted Onto Cart. Photo Taken By Gil Jeffer.

of-view calculations are necessary for lidar systems in understanding the connection between transmitter and receiver components. Knowing the telescopes field-of-view in comparison to the laser beam divergence helps in aligning these components to make accurate measurements. Also, having a beam expand too fast would be useless if one wants to study higher altitudes. The beam would become too weak at higher altitudes, which would provide small signal compared to background noise. In the same aspect, if the telescope's primary mirror is too small, the field-of-view would be smaller than the width and range of the backscattered signal. The telescope field of view can be calculated using simple geometric optics which is given by the equation:

$$\theta = \arctan(\frac{d/2}{f}) \tag{3.2}$$

where θ is the angle of view of the telescope, d is the diameter of the primary mirror, and f is the focal length of the telescope.

The laser beam divergence can also be calculated by using the formula:

$$\sin(\theta) = 1.22\frac{\lambda}{d} \tag{3.3}$$

in which θ is the angle of divergence of the beam, λ is the wavelength of the laser light, and d is the diameter of the beam as it exits the laser. A graph can be made to display the laser divergence within the field of view of the telescope, as shown below.

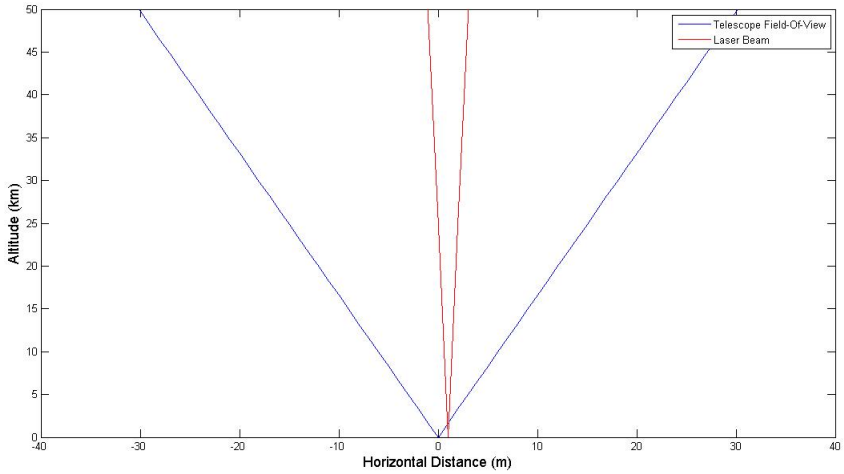

Figure 3.11 Telescope's Field-of-View up to 50 km.

Figure 3.11 portrays the laser light as it naturally diverges with comparison to the current 4inch receiving telescope field-of-view. As explained above, it is important to know the comparison of the beam divergence with the telescope field-of-view. Using the proper iris (eyepiece) in the lidar receiver setup should narrow the field of view until it nearly encompasses only the beam width. By narrowing the telescopes field-of-view to only the width of the beam is one of the crucial steps to allow for daytime collection. This will result in reduction of collecting photons that are not from lidar backscattering. Therefore, the only filtering of background noise will be done within the field of view that encompasses the beam. Polarizers will be used along with neutral density filters to block unwanted signal and not overflow

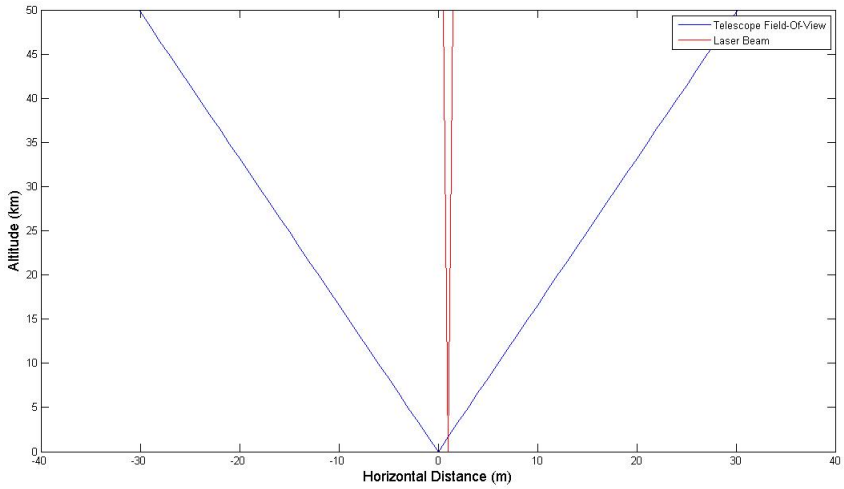

Figure 3.12 Telescope's Field-of-View up to 50 km with a 4x Beam Expander.

the photomultiplier tube.

The field-of-view depicted in Figure 3.12 is taken with the laser light passing through a beam expander. By using an expander, the beam is expanded by a factor of 4 while the telescope field of view remains constant. Notice the beam diverges slower as it travels through the atmosphere when a beam expander is present. This can be described by equation 3.3 and occurs due to the natural diverging property of light. There is an offset between the laser and the telescope, as shown in the Figures, which corresponds to the 1m separation between the two instruments on the optical table.

A snubber box is connected to the photomultiplier tube as shown in Figure 3.8. Snubbing is an important technique used in photon counting applications. Without some DC resistance between the anode and ground of the PMT, anode currents will charge the signal cable. A few hundred volts in the signal cable passing though a preamplifier may result in stored charge damaging the front end of the SR430. Snubbing also aids in reducing ringing, which is very common on photomultiplier tube outputs. Without a snubber correcting for ringing, the PMT may count multiple times for the same photon, providing inaccurate results. An illustration of the

effects of a snubber can be seen in Figure 3.13.

In addition, a snubbing device can reduce the reflections from the input to the preamplifier. The snubber box consists of two 26Ω potentiometers connected in series. This snubber setup was chosen over a standard 50Ω termination so that fine tuning may be performed to further reduce ringing and reflections in the signal.

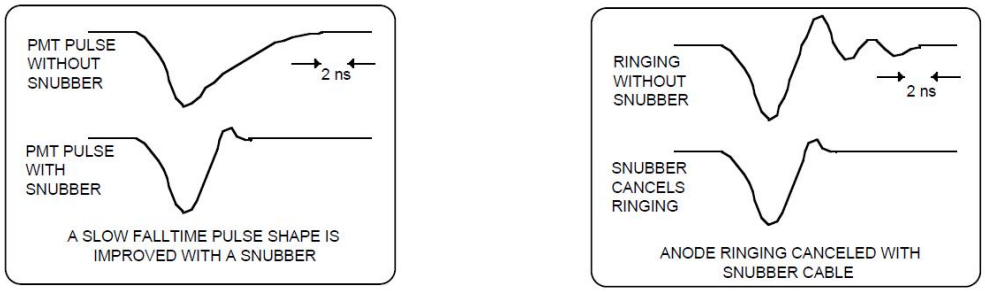

(a) **(b)**

Figure 3.13 Representations of an Observed Signal With and Without a Snubber Present in Regards to Rise/Fall Times and Ringing. [Stanford Research Systems et. al., 2007]

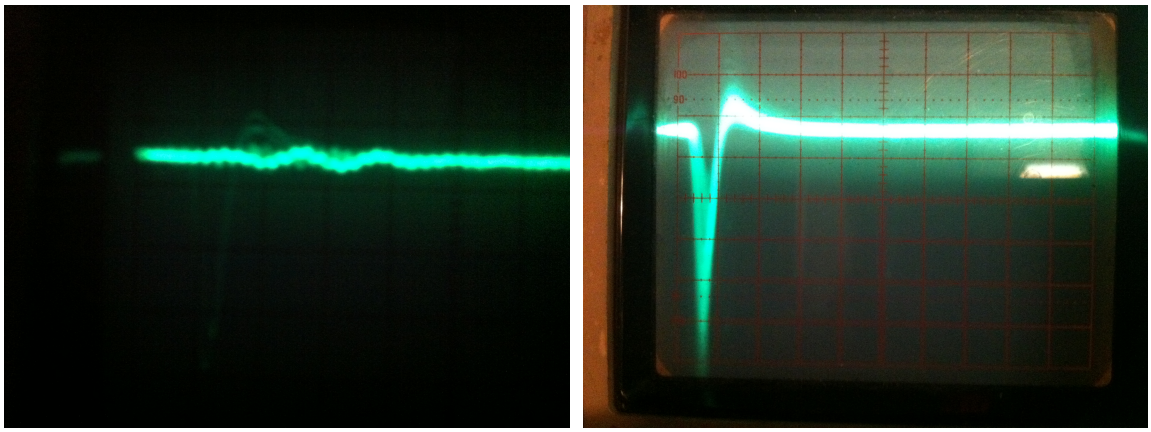

(a) Signal With Many Reflections **(b)** Ideal Signal

Figure 3.14 Observed Signals From the Oscilloscope.

Figure 3.14a shows an untuned snubber box that allows for many reflections in the signal cable. After proper tuning the ideal signal should look as in Figure 3.14b.

Although the NJIT lidar setup, due to the sensitivity of the photomultiplier, is

intended for nighttime observations only; daytime measurements can also be taken with a slight receiver optics change. Since the flux of light of the sun will flood any laser light pulses, polarization techniques need to be implemented. By using a polarizer in the optics tube that has the same polarity as the laser light pulses, the SR430 can collect light scattered from the laser and block unpolarized light from the sun, allowing for daytime measurements.

3.6 System Configuration

In order for proper measurements to occur, a series of preliminary operations must be completed to prepare the system. First, the photomultiplier tube must be cooled to reduce the amount of thermal counts collected. This ensures that most photon counts observed during the running of the lidar are from 532nm emission and not from the infrared spectrum. The cooler, as discussed in chapter 3, takes approximately 2 hours to fully reduce the temperature of the photomultiplier tube. Figure

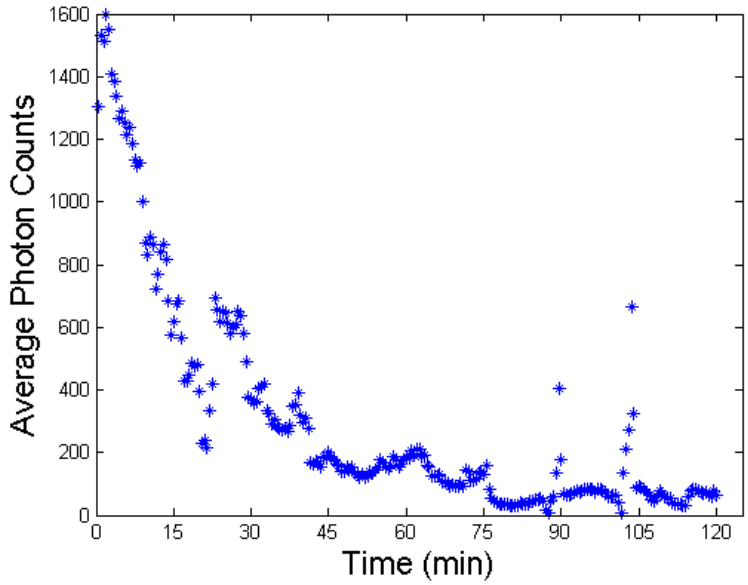

Figure 3.15 Cooling the Photomultiplier Tube Reduces the Amount of Thermal Noise Observed.

3.15 shows the reduction of thermal noise by cooling the photomultiplier tube and

measuring the average dark counts collected per 30 second interval. The small bumps in the data indicating higher number of received counts and the outliars at 90 and 105 minutes can be explained by a DC offset occurring when the cooler cycles on and off, as well as small shifts in the ambient room temperature. The minimum temperature the photomultiplier can reach is based on the ambient temperature of the environment. For a background temperature of 10^0C ambient, the pmt cooler cannot reduce the temperature below -25^0C. Figure 3.16 shows the temperature

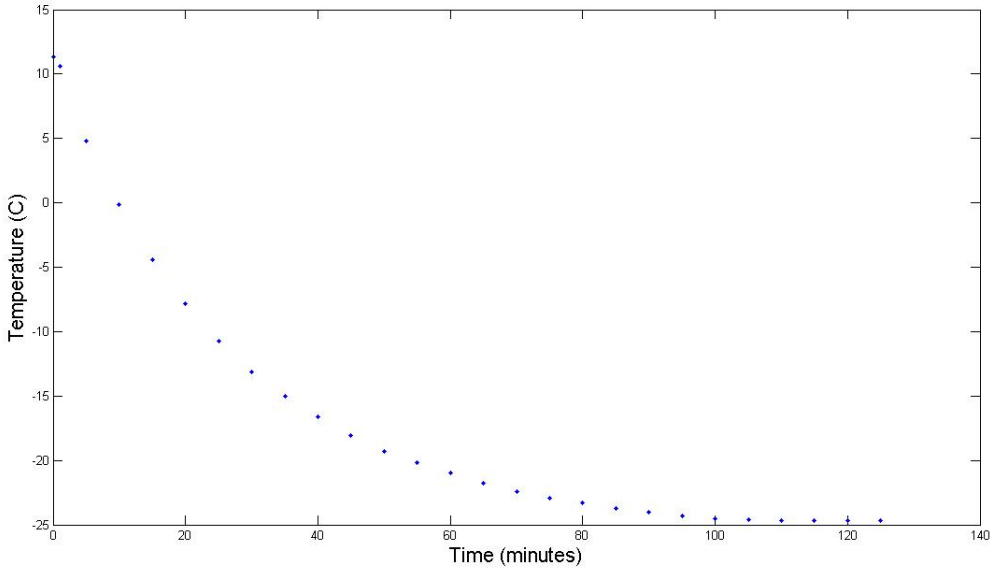

Figure 3.16 Temperature Profile of the Photomultiplier Tube as it is Being Cooled.

profile of the PMT as it is being cooled. It is important to note that the cooler must be set at a temperature lower than obtainable. Through observation, by setting an achievable cooling temperature, the cooler will automatically turn off. The temperature of the PMT will soon rise and the cooler will then turn back on. The power cycling of the cooler every 5-10 seconds shifts the DC bias, spiking the counts measured and contaminating the data as shown in Figure 3.15. The snubber, connected across the input of the SR430, needs to be properly adjusted to reduce reflections in the cable.

Only when the photomultiplier tube is cooled to the lowest temperature pos-

sible and the snubber adjusted can the discriminator level of the SR430 be set to disregard the electrical noise inherent in the system. At this point only real photons are counted by the SR430, and not system noise.

3.7 Data Processing

A MATLAB code, named Lidar Data Analysis Program is used to process the data, and is displayed in the appendix. The code begins by importing an ASCII file, which is a data file written by the labview program during data collection. The program then determines the size of the n x m data array, in which n correspond to the number of bins used and m the number of integration time cycles. A series of MATLAB commands obtains the time-stamp from the data, and is displayed in the bottom left corner of all processed data plots. The program computes the number of bins that will be considered the background, by taking the square root of n ($\sqrt{n}$), where n is the number of bins used during data collection. The program then finds the background, which is the mean of values of $n - \sqrt{n}$ to n. This background value, found for each interval, is subtracted from the photon count value in each bin. This method ensures that a mean background is found every 30 seconds, which takes into account sudden changes in background counts. After the data have been background subtracted, analysis such as mean counts per altitude, and contour plotting can be done.

CHAPTER 4

GRAVITY WAVES

4.1 Introductory Wave Mechanics

The equations, notations, and cited figures used in this chapter originate from *An Introduction to Atmospheric Gravity Waves* [Nappo et al., 2002]. A brief introduction of wave mechanics is necessary to understand how gravity waves function. A wave is a "self-sustaining disturbance of the medium through which it propagates" [Hecht et al., 2001]. An illustration of a wave is shown below.

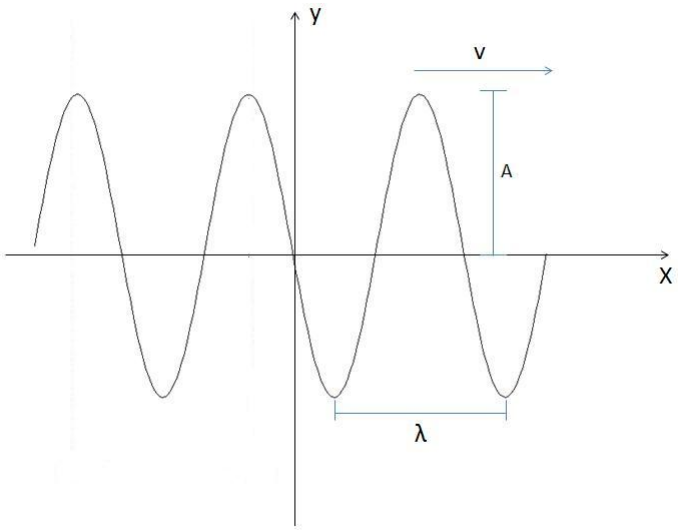

Figure 4.1 Graphical Representation of a Wave.

The figure shows a wave traveling at velocity v, having a wavelength λ, and an amplitude A. The frequency ω of a wave can be determined by the equation:

$$\omega = \frac{2\pi}{T} \tag{4.1}$$

in which T is the period of the oscillation of the wave. A convenient way to describe a wave is by wavenumber, given by:

$$k = \frac{2\pi}{\lambda}. \tag{4.2}$$

A wave is said to have a change of phase when the wave has shifted as illustrated in Figure 4.2. The solid line indicates the initial wave, and the dashed line shows

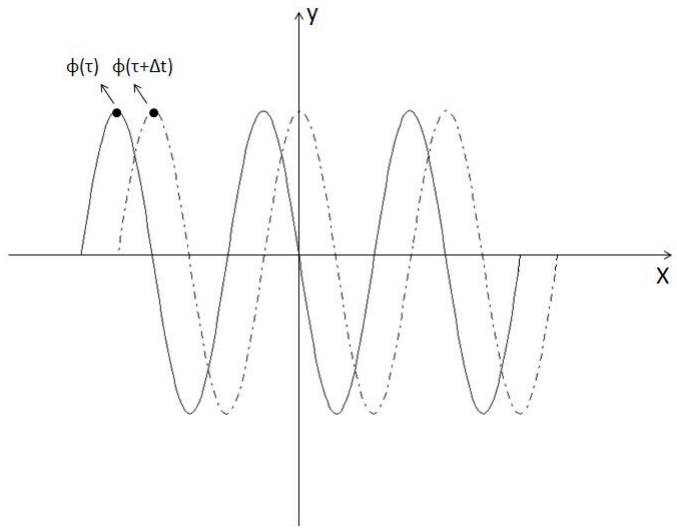

Figure 4.2 Phase of a Wave.

the new shifted position. The phase speed of the wave can be found by:

$$v_x = \frac{\omega}{k} \tag{4.3}$$

where ω is the angular velocity of the wave. In addition to wave speed, group velocity is rather important concept in gravity wave theory. The group velocity is the rate at which the pack of waves advance. It is the group velocity that transports energy through space [Nappo et al., 2002]. Looking at Figure 4.3 the wave as a whole travels with a group velocity, but individual wavelets may travel faster or slower than the actual wave. The group velocity in the x-direction can be calculated by:

$$v_g = \frac{\partial \omega}{\partial k} \tag{4.4}$$

For a given period T, long waves will travel faster than short waves and introduces a concept of wave dispersion. The relation between phase speed and wavenumber is called the dispersion relation. The name gravity wave may lead to the believe that

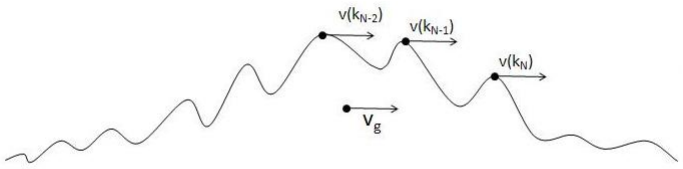

Figure 4.3 A Wave Moves With Group Velocity v_g But the Wavelets May Move At Different Phase Speeds. Figure Reproduced From [Nappo et al., 2002].

gravity is the restoring force of the parcel from its original position. It is buoyancy however, that acts to restore the wave to its equilibrium. Assume for a moment the atmosphere is at rest with a parcel of mass m_p at some altitude z_o. This parcel does not mix with the surrounding environment and the process is adiabatic, so that there is no net transfer of heat across the surface of the parcel. Now through some means (e.g. wind, pressure, particle collision) the parcel becomes displaced by an amount δz from z_o. The bouyant force can be written, using Newtonian mechanics, as:

$$\vec{F_b} = -g(m_p - m_a)\hat{z} \tag{4.5}$$

where m_a is the mass of air displaced by the fluid parcel and g is the acceleration of gravity, in which the positive direction is denoted upward. Using Newton's second law of motion, the above equation becomes:

$$m_p \frac{d^2(\delta z)}{dt^2} = -g(m_p - m_a) \tag{4.6}$$

The mass of each air parcel can be given as $m_p = \rho_p \nu_p$, where ρ_p and ν_p are the density and volume of the air parcel. The equation for state of dry air is the same as the ideal gas law

$$p = \rho RT \tag{4.7}$$

where R represents the universal gas constant (R = 287J $kg^{-1}K^{-1}$). Using the ideal gas law and the equation for the mass of the parcel, Newton's second law becomes:

$$\frac{d^2(\delta z)}{dt^2} = -g\frac{\rho_p - \rho_a}{\rho_p} = -g\frac{T_a - T_p}{T_a} \tag{4.8}$$

where δz is a slight change in altitude, p_a is the environmental air density, T_a is the environment temperature, and T_p is the parcel temperature. By expanding T_a and T_p to the first order, and noting that the initial temperature T_0 is greater than the change in environmental temperature per change in altitude, i.e.

$$T_0 \gg \frac{\partial T_a}{\partial z}\delta z \tag{4.9}$$

then equation 4.8 now becomes:

$$\frac{d^2(\delta z)}{dt^2} = \frac{-g}{T_a}(\frac{\partial T_a}{\partial z} - \frac{\partial T_p}{\partial z})\delta z \tag{4.10}$$

Making substitutions:

$$-\frac{\partial T_p}{\partial z} = \frac{g}{c_p} = \Gamma \tag{4.11}$$

and

$$\frac{\partial T_a}{\partial z} = \gamma_a \tag{4.12}$$

which are the adiabatic lapse rate Γ and atmospheric temperature gradient γ_a. Using these into equation 4.10 yields:

$$\frac{d^2(\delta z)}{dt^2} = \frac{-g}{T_a}(\Gamma - \gamma_a)\delta z \tag{4.13}$$

To continue this derivation, an equation for potential temperature needs to be used and is defined by:

$$\theta = T_a(\frac{p_0}{p})^{\frac{R}{(C_p)}} \tag{4.14}$$

in which p_0 is the pressure at the surface (usually 1000 millibars), p is the pressure at some altitude, and c_p is the specific heat at constant pressure. This equation is used to determine the temperature an air parcel would have if it went from an altitude of pressure p to pressure p_0. This temperature represents the air parcel experiencing an adiabatic process. Another important formula, the hydrostatic equation:

$$\frac{\partial p}{\partial z} = -\rho g \tag{4.15}$$

is based off of the hydrostatic approximation that assumes that a fluid has surfaces of constant pressure and density, and remains in this state throughout a horizontal layer of the atmosphere. By taking the logarithmic derivative of the potential temperature 4.14, and using ideal gas law 4.7 and hydrostatic equation 4.15, the result becomes:

$$\frac{1}{\theta}\frac{\partial \theta}{\partial z} = \frac{1}{T_a}(\frac{\partial T_a}{\partial z} + \frac{g}{c_p}) = \frac{\Gamma - \gamma_a}{T_a} \tag{4.16}$$

plugging 4.16 into 4.13 gives:

$$\frac{d^2(\delta z)}{dt^2} = \frac{-g}{\theta}\frac{\partial \theta}{\partial z}\delta z \tag{4.17}$$

Equation 4.17 describes simple harmonic motion of the parcel in the vertical direction. The general solution to the above equation is:

$$\delta z(t) = Ae^{iNt} + Be^{-iNt} \tag{4.18}$$

This solution depicts the motion of a parcel that has been displaced vertically and released. When N is real, it is known as the Brunt-Väisälä frequency, which is given by:

$$N = \sqrt{\frac{g}{\theta}\frac{\partial \theta}{\partial z}} \tag{4.19}$$

The Brunt-Väisälä frequency describes the frequency of oscillations of the air parcel.

When N is an imaginary quantity, there is said to be an instability, which is usually convective in nature. It is also important to look at the case in which the gravity wave is not traveling purely horizontally, but at an angle off of the horizontal. This causes the parcel to be moved on the same angle off the horizontal. The bouyant force acting on the parcel is:

$$\vec{F_s} = m_p \frac{d^2(\delta_s)}{\delta t^2} = -g \sin\beta (m_p - m_a) \tag{4.20}$$

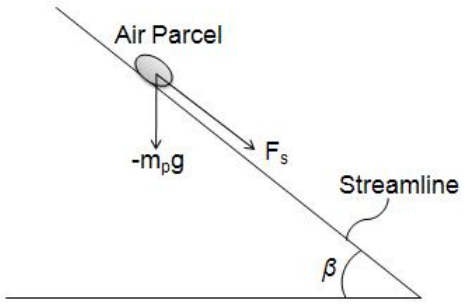

Figure 4.4 Air Parcel Displaced By Angle β. Figure Reproduced From [Nappo et al., 2002].

The $-g \sin\beta$ term in equation 4.20 finds the force due to gravity from a particular angle β. Figure 4.4 depicts the free body diagram of an air parcel moving in the direction of the streamline. Using the same method as shown before to find an equation of motion along a streamline, we have:

$$\frac{d^2(\delta s)}{dt^2} = \frac{-g}{\theta} \frac{\partial \theta}{\partial z} \sin^2\beta \delta s \tag{4.21}$$

The general solution to 4.21, the motion of the parcel along the streamline is:

$$\delta s(t) = Ae^{iN't} + Be^{-iN't} \tag{4.22}$$

where

$$N' = [\frac{g}{\theta}\frac{\partial\theta}{\partial z}\sin^2\beta]^{1/2} = N\sin\beta \tag{4.23}$$

When $\beta = 0$ the motion is completely in the horizontal direction. It is also important to point out that when the motion is completely horizontal there is no oscillatory motion, i.e. N' is also zero. Therefore it can be deduced that frequencies range between 0 and N depending on the angle β.

The equations for gravity waves from the Navier-Stokes equations are:

$$\rho\frac{D\vec{U}}{Dt} = -\nabla p + \rho\vec{g} \tag{4.24}$$

$$\frac{D\rho}{Dt} + \rho\nabla\cdot\vec{U} = 0 \tag{4.25}$$

$$\frac{DP}{Dt} - {C_s}^2\frac{D\rho}{Dt} = 0 \tag{4.26}$$

where

$${C_s}^2 = (\frac{c_p}{c_v})(\frac{p}{\rho}) \tag{4.27}$$

is the speed of sound and c_v is the specific heat capacity for dry air at constant volume. Equations 4.24, 4.25, 4.26, are the equations of conservation of momentum, conservation of mass and the conservation of thermal energy. The total derivative, $\frac{D}{Dt}$, can be described by the equation below.

$$\frac{D}{Dt} = \frac{\partial}{\partial t} + \vec{U}\cdot\nabla \tag{4.28}$$

The total derivative is used very often in atmospheric and oceanographic studies as a way to describe the motion of a fluid in different reference frames. Equation

4.28 describes a stationary observer watching the motion and behavior of the fluid, known as a Eulerian frame of reference. In a Lagrangian reference frame the observer follows along the motion of the fluid, and the total derivative can be shown as:

$$\frac{D}{Dt} = \frac{\partial}{\partial t} \tag{4.29}$$

which is equivalent to the definition of a partial derivative (in one dimension).

In addition to describing gravity waves, the above equations indicate the existence of acoustic waves. These acoustic waves, which are very abundant, cause problems when one tries to identify gravity waves. The solution is the Boussinesq approximation, which serves to eliminate the acoustic waves. The approximation starts by replacing $\rho = \rho_0 + \rho_1$ and $p = p_0 + p_1$ where 0 denotes the original value and 1 is the small perturbed value. Making this substitution into equation 4.24 yields:

$$(\rho_0 + \rho_1)\frac{D\vec{U}}{Dt} = -\nabla p_0 + \rho_0\vec{g} - \nabla p_1 + \rho_1\vec{g} \tag{4.30}$$

Assuming that the background state is in hydrostatic equilibrium, equation 4.30 becomes:

$$(1 + \frac{\rho_1}{\rho_0})\frac{D\vec{U}}{Dt} = -\frac{1}{\rho_0}\nabla p_1 + \frac{\rho_1}{\rho_0}\vec{g} \tag{4.31}$$

The Boussinesq Approximation makes the assumption that $|\frac{\rho_1}{\rho_0}| \ll 1$, which makes the fluctuations in the density affect buoyancy much more than the inertial term. Therefore the density fluctuations are only taken into account when combined with gravity g. "As demonstrated by Spiegel and Veronis et al. 1960, a result of the Boussinesq approximation is that the fluctuating changes in density due to local pressure variations are negligible. In this case we can treat the fluid as being incompressible, and acoustic waves eliminated [Nappo et al., 2002]." The result of

the Euler equations from the Boussinesq approximation are:

$$\frac{D\vec{U}}{Dt} = -\frac{1}{\rho_0}\nabla p + \frac{\rho_1}{\rho_0}\vec{g} \tag{4.32}$$

$$\nabla \cdot \vec{U} = 0 \tag{4.33}$$

$$\frac{D\rho}{Dt} = 0 \tag{4.34}$$

4.2 Linear Theory of Gravity Waves

Almost all the known information about the nature of gravity waves is derived from linear theory [Nappo et al.,2002]. It is best to begin describing gravity waves using a linear rather than a non-linear approach. It is much more trivial to imagine a linear flow and to describe its motion mathematically. In addition, large amounts of computing power is required to model and calculate complex non-linear systems. In a linearized theory of gravity waves (unlike non-linear), it is assumed that the background flow can be approximated by a mean flow. In addition perturbations need to be smaller than background atmospheric conditions, and waves cannot interact with other waves. Of course, these assumptions will not always hold true, since in the real atmosphere waves may interact in a non linear and non-monochromatic sense. However, using a linear approach to describe gravity waves is sufficient for depicting the motion and generation of gravity waves over a mountainous region.

4.2.1 Taylor-Goldstein Equation

The Taylor-Goldstein equation is the wave equation used to describe linear gravity waves. The Taylor Goldstein equation can be found by using the two dimensional Euler equations and then applying the Boussinesq approximation, which yields:

$$\frac{\partial u}{\partial t} + u\frac{\partial u}{\partial x} + w\frac{\partial u}{\partial z} = -\frac{1}{\rho}\frac{\partial p}{\partial x} \tag{4.35}$$

$$\frac{\partial w}{\partial t} + u\frac{\partial w}{\partial x} + w\frac{\partial w}{\partial z} = -\frac{1}{\rho}\frac{\partial p}{\partial z} - g \tag{4.36}$$

$$\frac{\partial u}{\partial x} + \frac{\partial w}{\partial z} = 0 \tag{4.37}$$

$$\frac{\partial \rho}{\partial t} + u\frac{\partial \rho}{\partial x} + w\frac{\partial \rho}{\partial z} = 0 \tag{4.38}$$

where u is the velocity of the fluid in the x-direction and w in the z-direction. Equation 4.35 is the equation for the momentum in the x-direction, and 4.36 describes the momentum in the z-direction. Equation 4.37 is the mass continuity equation, and 4.38 is an equation representing the conservation of thermal energy. The previous equations can be linearized by:

$$q(x, z, t) = q_0(z) + q_1(x, z, , t) \tag{4.39}$$

in which $q_0(z)$ is a value for a steady horizontal uniform background and $q_1(x, z, t)$ is a first-order perturbation. Assuming the background flow is in hydrostatic balance from equation 4.15, then equations 4.35-4.38 have the form:

$$\frac{\partial u_1}{\partial t} + u_0\frac{\partial u_1}{\partial x} + w_1\frac{du_0}{dz} = -\frac{1}{\rho_0}\frac{\partial p_1}{\partial x} \tag{4.40}$$

$$\frac{\partial w_1}{\partial t} + u_0\frac{\partial w_1}{\partial x} = -\frac{1}{\rho_0}\frac{\partial p_1}{\partial z} - \frac{\rho_1}{\rho_0}g \tag{4.41}$$

$$\frac{\partial u_1}{\partial x} + \frac{\partial w_1}{\partial z} = 0 \tag{4.42}$$

$$\frac{\partial \rho_1}{\partial t} + u_0\frac{\partial \rho_1}{\partial x} + w_1\frac{d\rho_0}{dz} = 0 \tag{4.43}$$

where ρ_0 is the background atmospheric density. By assuming wave-like solutions of the form:

$$u_1(x, z, t) = \tilde{u}(z)e^{i(kx-\omega t)} \tag{4.44}$$

$$\rho_1(x, z, t) = \tilde{\rho}(z)e^{i(kx-\omega t)} \tag{4.45}$$

$$p_1(x,z,t) = \tilde{p}(z)e^{i(kx-\omega t)} \tag{4.46}$$

$$w_1(x,z,t) = \tilde{\omega}(z)e^{i(kx-\omega t)} \tag{4.47}$$

and using the definition of the Brunt Väisälä frequency N^2 :

$$N^2 = -\frac{g}{\rho_0}\frac{\partial \rho_0}{\partial z} \tag{4.48}$$

a new set of equations can be found as:

$$i\Omega\tilde{u} - \tilde{w}\frac{du_0}{dz} = \frac{i}{\rho_0}k\tilde{p} \tag{4.49}$$

$$i\Omega\tilde{w} = \frac{1}{\rho_0}\frac{d\tilde{p}}{dz} + \frac{\tilde{\rho}}{\rho_0}g \tag{4.50}$$

$$ik\tilde{u} + \frac{d\tilde{w}}{dz} = 0 \tag{4.51}$$

$$i\Omega\tilde{\rho} + \tilde{w}\frac{\rho_0}{g}N^2 = 0 \tag{4.52}$$

These equations are known as the polarization equations because they give relative phases and amplitudes of various waves [Nappo et al. 2002]. Solving this set of equations for $\tilde{w}$ and noting that $\tilde{w}$ can be simplified as:

$$\tilde{w} = e^{\int 1/2H_s dz}\tilde{w} = e^{z/2H_s}\tilde{w} \tag{4.53}$$

becomes the Taylor-Goldstein equation [Nappo et al., 2002]:

$$\frac{d^2\hat{w}}{dz^2} + [\frac{k^2N^2}{\Omega^2} + \frac{k}{\Omega}\frac{d^2u_0}{dz^2} - k^2 - \frac{k}{\Omega}\frac{1}{H_s}\frac{du_0}{dz} - \frac{1}{4{H_s}^2}]\hat{w} = 0 \tag{4.54}$$

where Ω, the intrinsic frequency, is defined as $\Omega = \omega - u_0 k$. H_s is the scale height of the isothermal atmosphere. Equation 4.54 can be written in a more compact from by using prime notation for derivatives, and defining $\omega = \Omega + u_0 k$. The

Taylor-Goldstein equation now takes the form:

$$\frac{d^2\hat{w}}{dz^2} + [\frac{N^2}{(c-u_0)^2} + \frac{u_0''}{(c-u_0)} - \frac{1}{H_s}\frac{u_0'}{(c-u_0)} - \frac{1}{4{H_s}^2} - k^2]\hat{w} = 0 \tag{4.55}$$

In the above Taylor-Goldstein equation, the left most term in the brackets is known as the buoyancy term. The second is referred to as the curvature term. The third term is called the shear term and the fourth term is nameless, and is approximated small below the tropopause. The last term in the brackets of equation 4.55 is known as the nonhydrostatic term. It is refereed to as this because if the vertical perturbations are in hydrostatic balance, i.e: $\frac{\partial p_1}{\partial z} = -\rho g$, then this term would no longer appear in equation 4.55. The solutions to this Taylor-Goldstein equation can be solved using an analytic series or special functions (such as a Bessel), however, a simpler solution exists. In order to obtain this simple solution in terms of plane waves, the bracketed terms in equation 4.55 must be kept constant. In doing this, the general solution takes the form:

$$w_1(x,z,t) = \hat{w}(z)e^{\frac{z}{2H_s}}e^{i(kx-\omega t)} \tag{4.56}$$

4.2.2 Solution to the Taylor-Goldstein Equation With Constant Background Wind Speed

Now that a simple solution has been found to the Taylor-Goldstein equation, it is important to find the solution when a constant background wind speed is present. Starting from the Taylor-Goldstein equation with the form:

$$\frac{d^2w}{dz^2} + [\frac{k^2N^2}{\Omega^2} - k^2]\hat{w} = 0 \tag{4.57}$$

and the formula for vertical wavenumber is:

$$m = \pm[\frac{k^2N^2}{(\omega - u_0k)^2} - k^2]^{1/2} \tag{4.58}$$

using the substitution $\Omega = \omega - u_0k$ and solving for ω:

$$\omega = u_0k = [\frac{N^2k^2}{m^2 + k^2}]^{1/2} \tag{4.59}$$

Using our solution for ω above, and equations $c_x = \frac{\omega}{k}$ and $c_z = \frac{\omega}{m}$, yield the phase velocities:

$$c = u_0 + \frac{N}{k}\cos\beta \tag{4.60}$$

$$c_z = u_0\frac{k}{m} + \frac{N}{m}\cos\beta \tag{4.61}$$

The group velocities can also be found, by taking the derivative of ω with respect to k and m:

$$u_g = \frac{\partial\omega}{\partial k} = u_0 + \frac{m^2}{N^2}(c - u_0)^3 \tag{4.62}$$

and

$$\omega_g = \frac{\partial\omega}{\partial m} = -\frac{km}{N^2}(c - u_0)^3 \tag{4.63}$$

4.2.3 The WKB Method

The Taylor-Goldstein equation provides a plane wave solution only when the atmospheric variables are constant. What if u_0 and N slowly change with time? A new approach must be taken, known as the WKB method. Start with the differential equation:

$$\frac{d^2\psi}{dz^2} + Q^2(z)\psi = 0 \tag{4.64}$$

This equation can be solved using the WKB method when $Q(z)$ is slowly changing. The WKB solution is:

$$\psi(z) = \psi_0 Q^{-1/2} e^{\pm i \int_0^z Q dz} \tag{4.65}$$

where ψ_0 is constant. The solution 4.65 satisfies the equation:

$$\frac{d^2\psi}{dz^2} + Q^2(z)(1+d)\psi = 0 \tag{4.66}$$

in which

$$d = \frac{1}{2Q^3}\frac{d^2Q}{dz^2} - \frac{3}{4Q^4}(\frac{dQ}{dz})^2 \tag{4.67}$$

Note that when $d \ll 1$ then 4.66 approaches the Taylor-Goldstein equation previously discussed. The WKB method is used very frequently in atmospheric studies, and assumes the wave perturbations are in hydrostatic equilibrium.

4.3 Terrain-Generated Gravity Waves

"The linearized equations of motion predict that the vertical displacement of a stably stratified flow almost always leads to the generation of gravity waves [Nappo et al., 2002]." The same is true when the air flow needs to travel past terrain obstacles such as ridges, hills and mountains. In addition to physical obstacles, terrain depressions such as canyons, basins, and valleys can also become a generator of gravity waves. The amplitudes of the terrain generated gravity waves are proportional to the amplitudes of the terrain. Although most gravity waves decrease in amplitude as they propagate upward into the atmosphere, under certain conditions can the opposite be true. In this case the wave will eventually break, which is known as clear air turbulence. An analogy to this is waves breaking on a beach. As the wave approaches the shore, its amplitude increases and crashes on the shoreline. The simplest mountain wave case is a uniform two-dimensional flow with a constant Brunt-Väisälä frequency over a raised terrain.

Figure 1.2 illustrates the flow over a ridge, which generates mountain waves. Since mountain waves are generated near the surface, by passing over a ridge, the waves transport energy upward as they propagate. Therefore, the horizontal group velocity has to be negative, and the vertical group velocity positive. In addition, the vertical wavenumber m has to also be negative. This means that the wavefronts must be moving downward. To begin to solve for waves over a ridge, consider an equation for surface height, given as:

$$h(x) = He^{ik_s x} \tag{4.68}$$

where H is the amplitude of the ridge, and $k_s = \frac{2\pi}{\lambda_s}$ in which λ_s is the wavelength of the ridge. In the case of constant background wind and stratification, the Taylor-Goldstein equation takes the form:

$$\frac{d^2\hat{w}}{dz^2} + [\frac{N^2}{{u_0}^2 - k^2}]\hat{w} = 0 \tag{4.69}$$

when $\frac{N^2}{{u_0}^2} > k^2$, the solution to 4.69 is

$$\hat{w}(k, z) = Ae^{-imz} \tag{4.70}$$

where $m^2 = \frac{N^2}{{u_0}^2} - k^2$. Proper treatment of the boundary conditions are necessary. At the upper limit, the radiation condition needs to be applied. The radiation condition assumes only upward propagating wave energy is allowed, which ensures that all energy above the boundary can not be reflected down. The constant A can be found to be:

$$A = \hat{w}(k, 0) = i2\pi u_0 k H \delta(k - k_s) \tag{4.71}$$

where δ is the Dirac Delta function of $k - k_s$. The equation for the surface streamline

is:

$$\phi = z - h(x) \tag{4.72}$$

The unit vector normal to the streamline can be found as:

$$\hat{n} = \frac{\nabla\phi}{|\nabla\phi|} = \frac{-\frac{dh}{dx}\hat{x} + \hat{z}}{|\nabla\phi|} \tag{4.73}$$

The phase speed and group velocity can be found for a wave moving over a surface corrugation.

$$c_x = \frac{\omega}{k} = u_0 \pm \frac{N}{(k^2+m^2)^{1/2}} = u_0 \pm u_0 \tag{4.74}$$

Since it has already been discussed that the horizontal phase speed is zero ($c_x = 0$), the negative branch of the above equation must be used. The vertical phase speed is:

$$c_z = \frac{\omega}{m} = u_0\frac{k}{m} - \frac{N}{(k^2+m^2)^{1/2}} = 0 \tag{4.75}$$

The phase speeds above are for a reference frame that is attached to the terrain. The phase speeds relative to the flow are:

$$c_x = -u_0 \tag{4.76}$$

$$c_z = -\frac{u_0 k}{m} \tag{4.77}$$

From the above equations, it can be deduced that the wave fronts seem to be traveling downward and upstream. The horizontal group velocity (for a terrain attached reference frame) is:

$$u_g = \frac{\partial\omega}{\partial k} = u_0 + \frac{\partial\Omega}{\partial k} \tag{4.78}$$

Using the negative branch of the dispersion relation, and $\Omega = -u_0 k$, the horizontal

group velocity now becomes:

$$u_g = u_0 \frac{k^2}{k^2 + m^2} \tag{4.79}$$

The vertical group velocity is:

$$w_g = \frac{\partial \omega}{\partial m} = u_0 \frac{km}{k^2 + m^2} \tag{4.80}$$

The energy therefore is transported upward and downstream. Figure 4.5 shows wavefronts, wave vector and group velocity vector over a surface ridge.

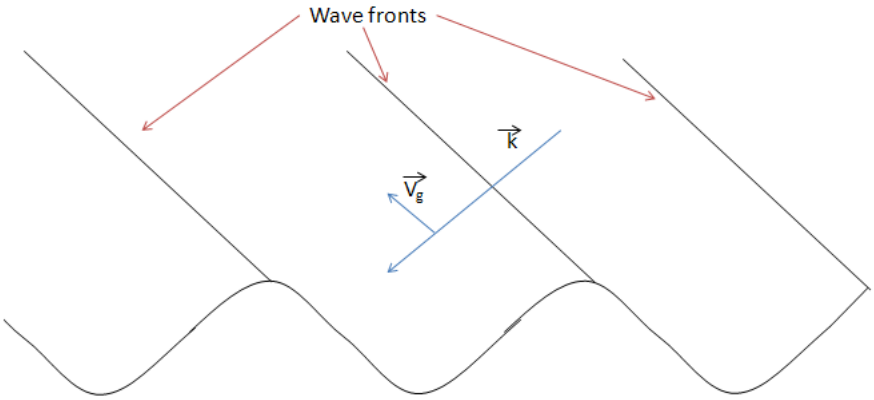

Figure 4.5 Wave Fronts, Wave Vector (k), and Group Velocity Vector(V_g) Over a Surface Corrugation. The Transport of Wave Energy Determines the Tilt of the Wave Fronts. This Figure is a Representation From [Nappo et al., 2002].

4.3.1 Three Dimensional Mountain Induced Gravity Waves

Although the research conducted in this thesis does not include treatment of three-dimensional gravity waves, it is an essential topic to summarize. To solve for the case of a three-dimensional mountain, the y-dimension needs to be added into the Taylor-Goldstein equation. The Taylor-Goldstein equation now takes the form:

$$\frac{d^2\hat{w}}{dz^2} + [\frac{(k^2 + l^2)N^2}{(ku_0 + lv_0)^2} - \frac{ku_0'' + lv_0''}{ku_0 + lv_0} - (k^2 + l^2)]\hat{w} = 0 \tag{4.81}$$

in which l and v_0 are the wavenumber and background wind speed in the y-direction. The horizontal perturbation velocities (obtained from polarization equations, not discussed here) are given by:

$$\hat{u_1}(k,l,z) = \frac{ik}{k^2+l^2}[\frac{l\hat{w}(lu_0{}' - kv_0{}')}{k(ku_0+lv_0)} + \frac{d\hat{w}}{dz}] \tag{4.82}$$

and

$$\hat{v_1}(k,l,z) = \frac{-il}{k^2+l^2}[\frac{k\hat{w}(lu_0{}' - kv_0{}')}{l(ku_0+lv_0)} + \frac{d\hat{w}}{dz}] \tag{4.83}$$

Two-dimensional ridge solutions can also be found using these equations by setting $l = 0$. For constant background wind speed, 4.81 becomes:

$$\frac{d^2\hat{w}}{dz^2} + [\frac{(\kappa_H^2)N^2}{(ku_0)^2 - (lv_0)^2} - k_H^2]\hat{w} = 0 \tag{4.84}$$

where κ_H is the projection of the wave vector onto the horizontal plane. Using the hydrostatic approximation and taking the background wind in the x-direction to be zero, 4.84 reduces to:

$$\frac{d^2\hat{w}}{dz^2} + \frac{(\kappa_H^2)N^2}{ku_0{}^2}\hat{w} = 0 \tag{4.85}$$

using equations 4.62 and 4.63, and noting that $\Omega = -ku_0$, the group velocities can be found as:

$$u_g = u_0\frac{l^2}{\kappa_H^2} \tag{4.86}$$

for the x-direction, and:

$$v_g = \frac{\partial\Omega}{\partial l} = -u_0\frac{kl}{\kappa_H^2} \tag{4.87}$$

$$w_g = \frac{\partial\Omega}{\partial m} = \frac{u_0{}^2k^2}{N\kappa_H} \tag{4.88}$$

for the y and z directions respectively.

CHAPTER 5

LIDAR CAMPAIGNS AND DATA ANALYSIS

5.1 The Jeffer Observatory

Construction of the Jeffer Observatory began at UACNJ in the summer 2009 while an undergraduate. The observatory will contain a 48inch ITEK telescope, and will be used in place of the 4inch Meade telescope on the tropo-strato lidar system. The ITEK telescope, pictured in 5.1, was modeled using the lidar equation and will increase the accuracy of the system greatly, allowing for measurements up through the mesosphere.

Figure 5.1 Photo of the 48inch ITEK Telescope. Photo Taken by Personnel of Starfire Optical Range at Kirkland AirForce Base, New Mexico.

When construction is finished, the Jeffer Observatory will look like Figure 5.2 and will open/close via rail system. Excavation of the land for the observatory began in September 2009. After excavation of the terrain, quarry process was inserted in locations below the area where the telescope and electronics shed will be, as depicted in Figure 5.3. Concrete forms were made, with rebar placed in-between, which provide a sturdy concrete foundation for the observatory. Concrete was filled in the forms and let set for several days. Afterwards a concrete slab was made that would allow construction of electronics shed to begin. Figures 5.4 and 5.5 show photos of the construction process.

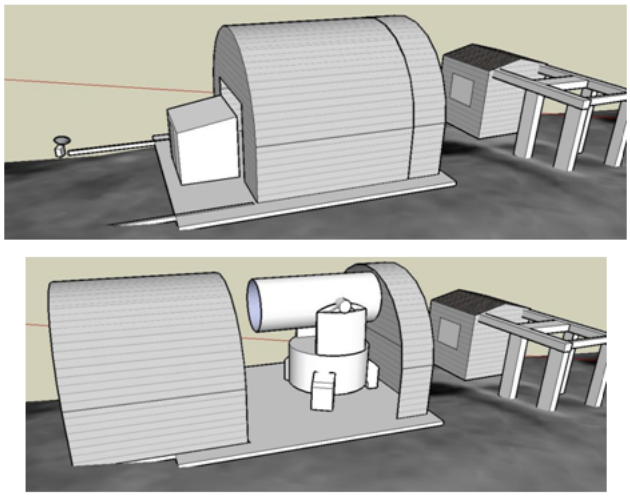

Figure 5.2 Final Design of the Jeffer Observatory. The White Shed Next To the Observatory Will Be the Telescope's Electronics Shed. Image Created By Andrew Gerrard.

(a) **(b)**

Figure 5.3 (a) Excavation. (b) Quarry Process Is Compacted Over Regions Where the Telescope and Electronics Shed Will Be Mounted. Photos Taken By Members of the United Astronomy Clubs of New Jersey.

Lack of funding for the rails led to the halt on construction of the Jeffer Observatory in early summer 2010. In the meantime preparations were made to start running the lidar system without the 48inch ITEK telescope.

5.2 Experimental System Observations and Obstacles

A calorimeter was obtained in late May 2010 which allowed for tuning to maximize the laser's output power. Several attempts at optimizing power out of the third

(a) **(b)**

Figure 5.4 (a) Forms Built With Rebar Inside. (b) Concrete Foundation Before Slab Was Made. Photos Taken By Gil Jeffer.

Figure 5.5 Concrete Slab With Electronics Shed

harmonic oscillator (355nm light) led to a maximum power reading of 200mW. The factory's output power specification for the 3rd harmonic is 2W, 10x the power the laser was producing. To comply with the manufacturer's warranty, the 3rd harmonic oscillator was then shipped back to the company for repair. After diagnosis from the company, it was the crystals coating wear that was the cause of the decreased output power. This was due to storing the laser outside in a shed prior to bringing it inside a temperature and humidity controlled setting. The 3rd harmonic was

fixed and delivered back late October 2010. Extreme cold, snow, and other weather conditions put lidar campaigning on hold until March 2011.

A lidar campaign took place in mid March 2011. Within a few hours of the laser operating the laser's power supply made several loud sounds followed by sparking. The laser was immediately powered down, and diagnosis was nearly impossible due to the complexity of the inner circuits of the power supply. The laser was sent out for repair in early April and returned to New Jersey Institute of Technology in November 2011. Shipment of the laser from NJIT to the field site occurred in late January 2012. During the March 2011 campaign it was observed that the system was collecting an unusually small number of counts. Diagnosis of the system and each component was performed to determined the cause. The diagnosis pointed to a problem relating to the photomultiplier and further investigation led to the discovery of a Plexiglas PMT window. Looking at the specifications of the PMT window, shown in Figure 5.6, one can see the transmission of light at 355nm is low in Plexiglas, at about 50%. The window needed to be replaced, in order to allow higher transmission of ultraviolet light into the PMT. This would corrected for the low amount of collected photon counts.

Dark count measurements prior to early February 2012 had to be discarded due to light leaks in the photomultiplier housing shutter. The first set of true dark count measurements were taken on February 18th 2012. The plot, Figure 5.7, is an average count per bin for a total collection time of 2 hours. As seen from the figure, the system is experiencing a significant amount of periodic noise. To trace the source of this noise a Signal Hound was acquired. The noise frequency observed was 770kHz, a local AM band radio station. Removing the periodic noise from the system was a goal, however, proper removal from the data processing is an alternative solution.

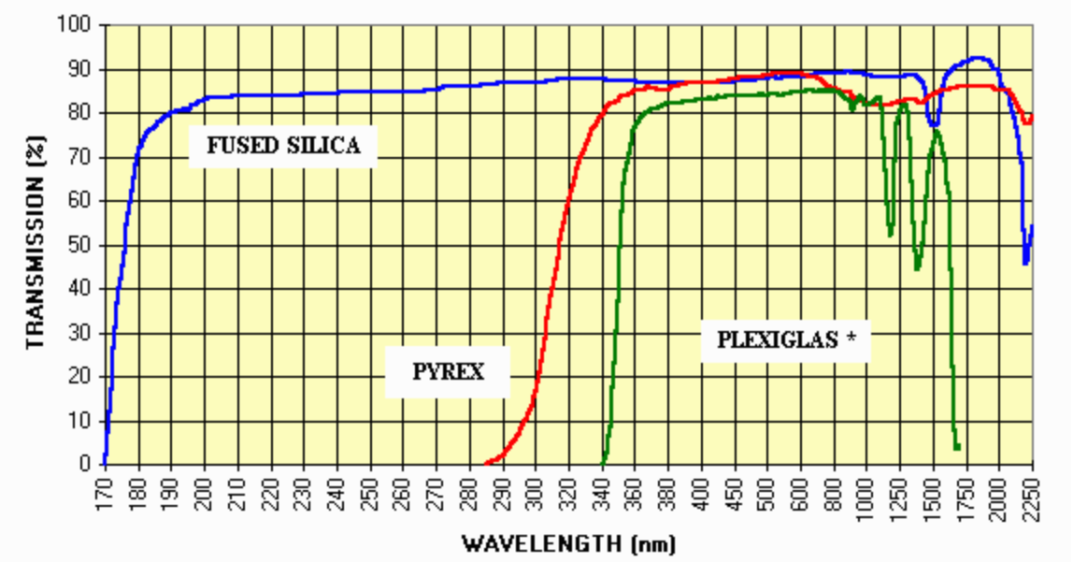

Figure 5.6 Transmission Percent per Wavelength of Plexiglas Photomultiplier Window. [Products For Research Inc. et al., 2012]

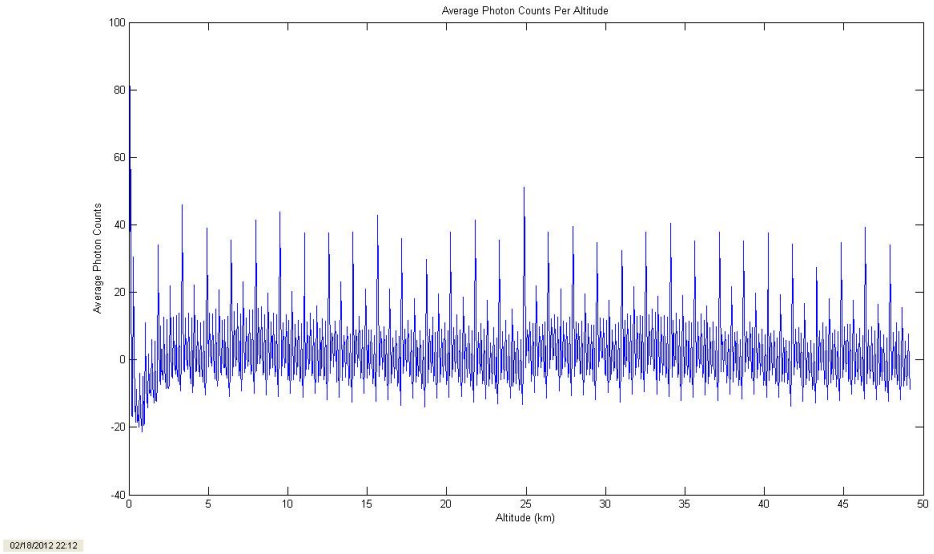

Figure 5.7 System Noise Observed on February 18th 2012.

5.3 A Switch From 355nm to 532nm

While measuring dark counts, the laser was re-tuned again to achieve maximum output power on the third harmonic oscillator before campaigning began. Attempts to maximize output of the laser by rotating the wave-plates and tuning the crystals were unsuccessful. After several days of troubleshooting, the third harmonic oscil-

lator was taken off of the lidar system. The system now only uses a 2nd harmonic oscillator that outputs light in the visible at 532nm.

Since the lidar forward model is wavelength and power dependent, a comparison of the estimated return counts between the the old setup (355nm) and new (532nm) should be done. The expected return counts per altitude for a 2W 355nm laser can be shown in figure 5.8.

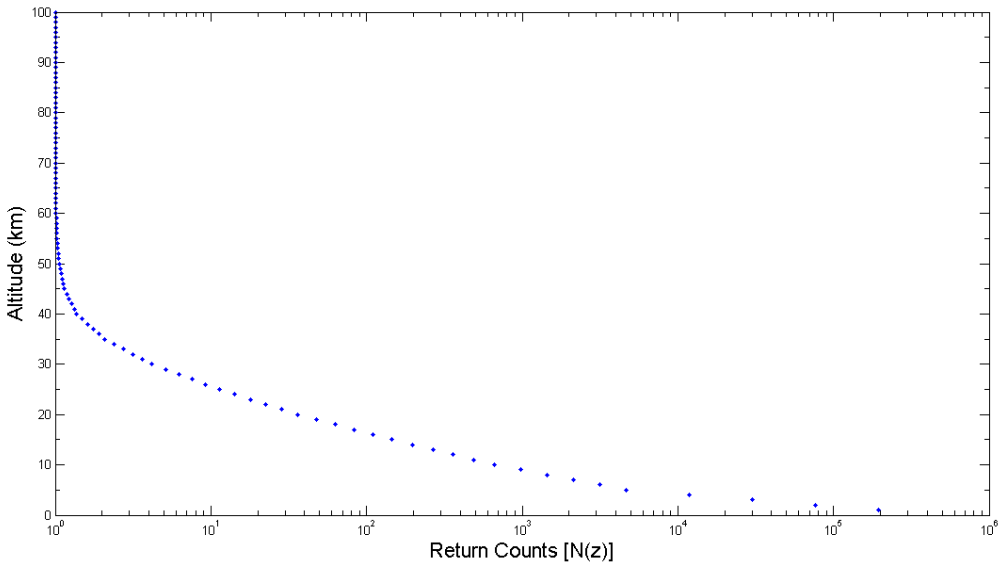

Figure 5.8 Expected Number of Backscattered Photons per Altitude Using a 2W 355 nm Laser.

In comparing the expected return counts between a 2W 355 nm laser shown in figure 5.8 and a 4W 532 nm laser depicted in Figure 2.1, there is a large difference in counts at lower altitudes. In addition, starting above approximately 35 km, the return counts of the 355 nm laser decrease greater in comparison to the 532 nm laser. This difference in return counts can be explained by the lidar equation, which multiplies the laser power and wavelength, and also accounts for backscatter cross section and transmittance through the atmosphere, which are both wavelength dependent. In terms of understanding the physics, the 532 nm light can be expected to have larger returned photon counts at higher altitude due to the transmittance

of the atmosphere. The Earth's atmosphere allows nearly all visible light to pass through, whereas ultraviolet radiation is greatly absorbed. In addition, the second harmonic (532 nm) has an output power of double the third harmonic (355 nm), at 4W compared to 2W, which allows for more backscattering to occur. Looking at the percent error of a 2w 355 nm, depicted in Figure 5.9, the percent error is half that of the 355 nm laser (from Figure 2.2). Therefore, in addition to having more expected return photon counts, using a 4W 532 nm laser result in the lidar equation being twice as accurate than in the 2W 355 nm case.

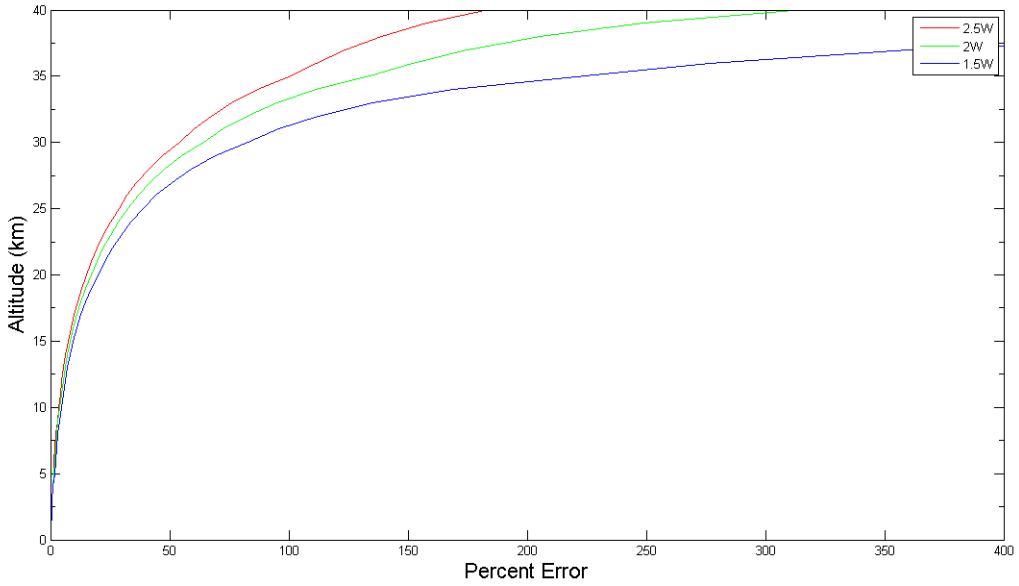

Figure 5.9 Lidar Percent Error with 4inch Telescope for Multiple Laser Powers of a 355nm Laser.

5.4 March 23rd 2012

March 23rd 2012 was the first day of campaigning and first light data was obtained. The data, shown in Figure 5.10 offered the possibility of poor alignment of the telescope and laser.

The very large number of counts at low altitude, coupled with the few counts from higher altitudes, suggested that the laser was not well aligned with the receiving

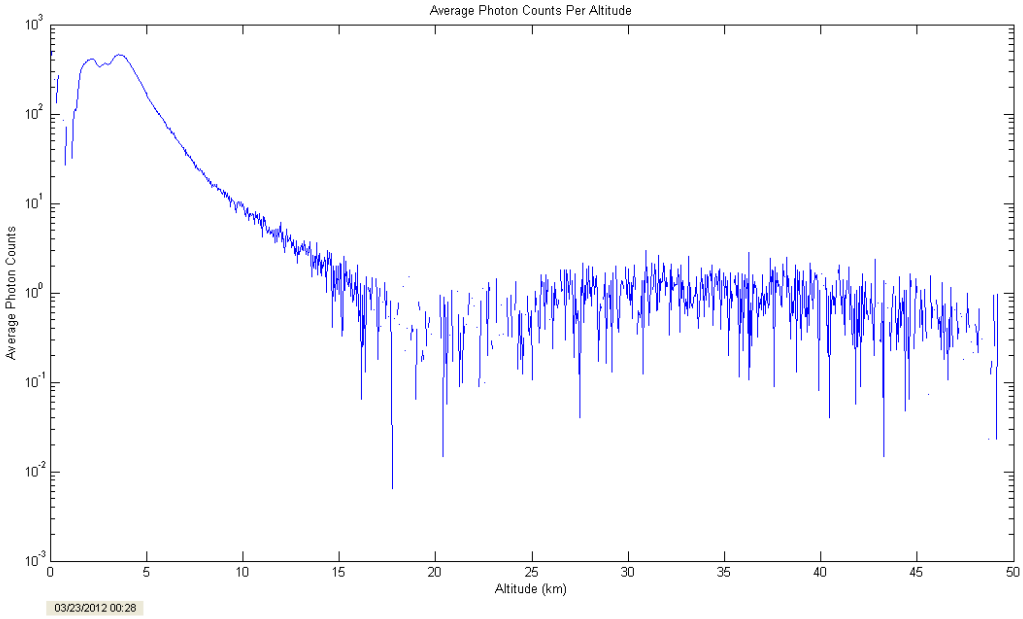

Figure 5.10 Lidar Observations from March 23rd 2012.

optics. It was suggested that the photons observed might be artifacts caused by secondary scattering of the beam by the atmosphere. In an effort to expand the field of view and make exact alignment less critical the center collimation tube inside the telescope was removed, shown in Figure 5.11b.

(a) **(b)**

Figure 5.11 The Left Image Depicts the Center Collimation Rod on the Telescope Before Cutting. The Right Image Shows the Top Portion of the Telescope Collimation Rod Cut.

5.5 April 14th 2012

A new set of data was collected on April 14th 2012. This data, represented the first of data after removing the collimation rod, as shown in Figure 5.12, and seemed promising. Upon further investigation in the loglog scale, there seemed to be a large number of counts being collected in the region of the upper troposphere (10 km), suggesting that the lidar system was not functioning properly. From looking at the figure, extremely high photons counts can be observed at low altitudes, corresponding to a few hundred nanoseconds after the laser pulses. The rapid drop in counts followed by a recovery period suggested the possibility of PMT saturation.

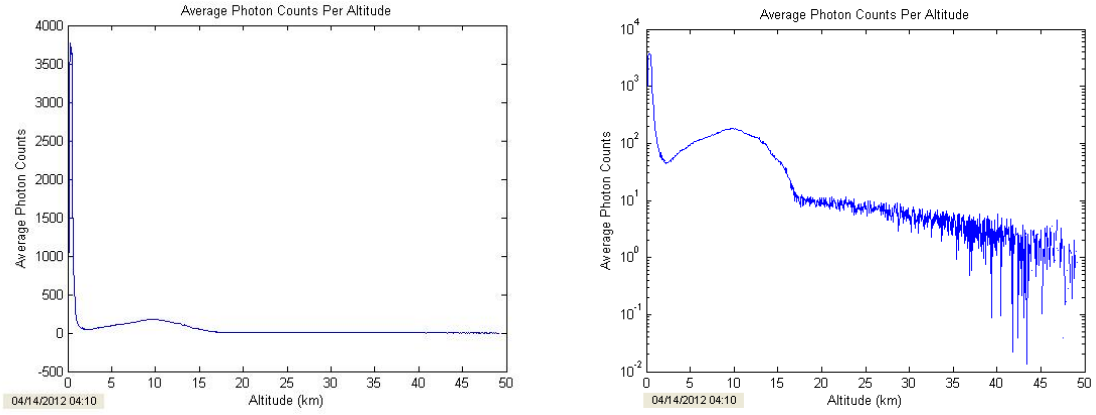

(a) **(b)**

Figure 5.12 Data Taken on the Night of April 14th 2012.

Several tests following the April 14th campaign were done to ensure that it was the photomultiplier that was causing the noise. The first test was to decrease the aperture area of the receiver, therefore allowing less light to enter the photomultiplier and reduce the chance to saturate. The PMT shutter was used to block portions of light. However, when closing the shutter all the way, it was observed that the SR430 was still characterizing the counts the same as in Figure 5.12. Therefore, it was not the photomultiplier that was being saturated, but noise generated by another instrument, or a source nearby. A few days later upon inspection of the lidar with Dr. Gerrard, it was found that the pre-amplifier was the source of the

response observed. The pre-amplifier was continuously overloaded from the amount of photons collected from the photomultiplier. Dr. Gerrard's recommendation was to remove the pre-amplifier and take more measurements.

5.6 April 29th 2012

The next night of campaigning occurred on April 29th 2012. This night looked promising because the pre-amplifier was removed, and the indoor background sampling returned positive results. After plotting the data, the results from the log of average photon counts appeared normal, as depicted in Figure 5.13.

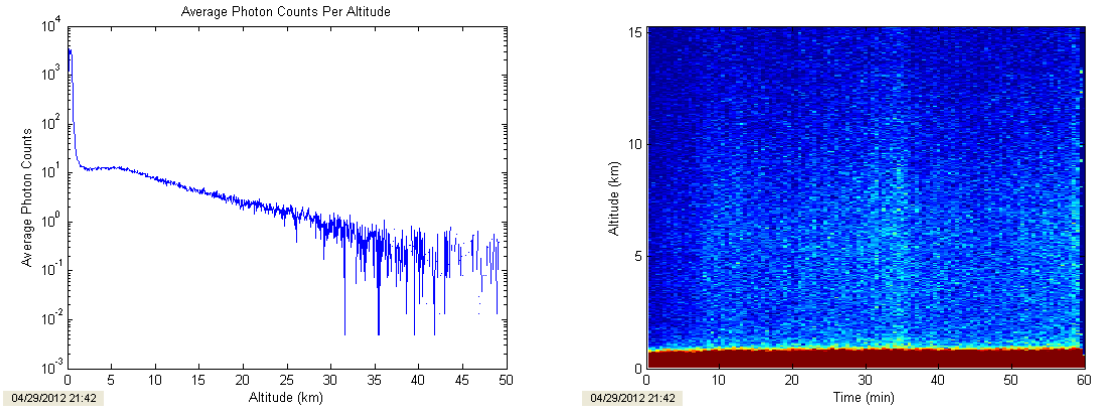

(a) **(b)**

Figure 5.13 Data Taken on the Night of April 29th 2012.

Creating a contour image of the data however showed undesirable structure. This structure, after further analysis thought to be from an improper choice in discriminator levels. By choosing an improper discriminator level, photons could be double counted and even triple counted due to reflection in the cabling. This was the first conclusion to why the speckle patterns appeared in the contour image. Further investigation on May 14th, 2012 led to the conclusion that it was the snubber box that was the cause of this noise, and not an improper discriminator level as first suspected. The snubber, if not properly assembled and tuned, can allow for signal ringing in the cabling. This ringing affect can be recorded as additional,

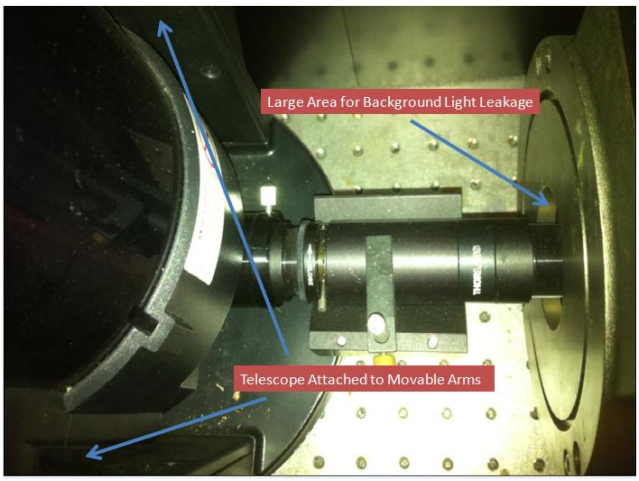

Figure 5.14 Old Mount Used to Secure the Receiver Optics.

false counts by the SR430, leading to faulty data. In response, it was suggested snubber assembly need replacement. In addition, the current receiver optics mount made consistent alignment impossible. The telescope mount was not sturdy, and the telescope could easily change position during measurements. It was determined that the photomultiplier tube housing was not properly light sealed, allowing background light to enter the tube. While re-creating the snubber, it was also essential to create a sturdy receiver optics mount. This mount would not allow for the telescope or optical tube to move, as well as be light-tight.

The original telescope mount, and the optical tube connection to the PMT can be seen in Figure 5.14. As shown in the figure, the large gaps from the connection between the optics tube and the photomultiplier tube housing, allows for significant light leakage. In addition, the original telescope mount cannot be bolted to the optical bench, and the arm allows for rotation of the telescope. The telescope was easily misaligned, from bumps and motion of the optical bench. To solve this, a replacement mount was designed, with the help of Dr. Melville and Gil Jeffer, and bolts solidly to the optical bench in a fixed alignment. Alignment of the laser and the receiving telescope is achieved by adjustment of the verniers on the laser's turning mirror. The design would look like figure 5.15.

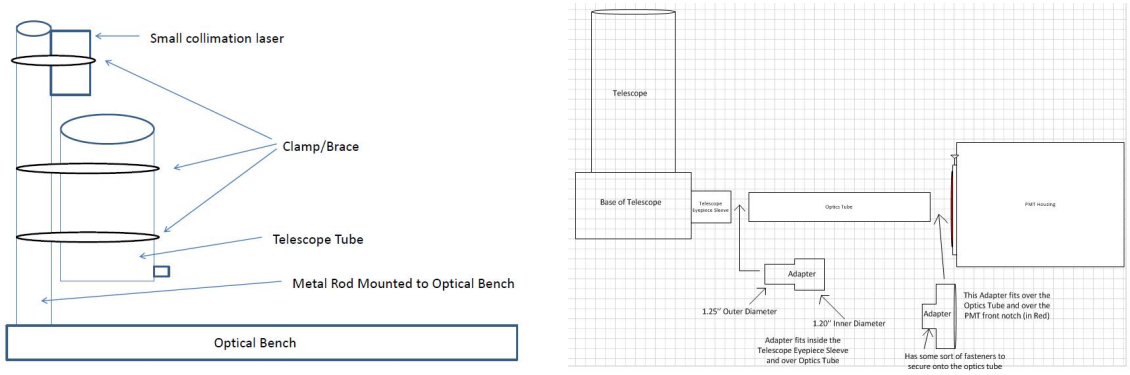

(a) **(b)**

Figure 5.15 Designs for a New Receiver Optical Mount.

As initially designed, a single metal rod is fixed to the optical table, the receiver telescope and a small laser are mounted to the rod by clamps. The laser would serve to help in collimation of the telescope and the receiver optics tube, and to verify the beam is not distorted exiting the optics tube. Two adapters would also be made, one to secure the telescope to the optics tube, and another to secure and align the optics tube into the PMT chamber, as shown in Figure 5.15b. This initial design, was modified before fabrication, and is shown in figure 5.16. Two 1 inch aluminum

(a) **(b)**

Figure 5.16 New Receiver Optics Mount Attached to the Lidar Optical Table.

rods were implemented, rather than one, to increase the sturdiness of the mount.

The two boards securing the telescope were machined from delrin sheets. 1/4-20 Set screws and reinforcement rods provided additional sturdiness. An adapter

was needed to fill the gap caused by differing diameters of the telescope eyepiece holder and the optics tube. It was fabricated from a thin plastic tube, that fit inside the telescope eyepiece sleeve, and over the optics tube. The adapter holding the optics tube to the PMT housing is also made of delrin, and has a boss on the inside of the adapter that allows for a snug fit onto the photomultiplier tube housing. This configuration resolves light leakage problems, and securely aligns the optical components. The new snubber was created using a 12-turn 50Ω potentiometer, and a 10 inch RG174/U coax cable, as recommended in the SR430 manual. With the addition to the new mount and snubber, the lidar is ready for night-time observations.

CHAPTER 6

CONCLUSIONS AND OUTLOOK

The July 3rd 2012 campaign was the first campaign that utilized the new receiver optics mount and the replacement snubber. While diagnosing the system before running, a new discriminator level, and alignment were made. In addition, the high voltage power supply was changed from 1500V to 2100V. This increase in voltage to the photomultiplier tube allowed the PMT to become more sensitive to incident photons but not high enough to damage the instrument. The image of the data collected on July 3rd is shown in Figure 6.1. The large time of no available data is due to a power outage at the field site. The lidar data collection continued running off of a generator until power returned to the field site. As shown by Figure 6.1, the system still has inherent noise, due to the random dense blotches in the image. It is unclear what caused the large density of counts observed near 4 km at the 40-60 minute time. This feature is not physical and is likely due to an improper functioning of the lidar around this time. Upon further investigation of the data there seems to be some wave activity around 3.5-4.5 hours local time at the 5-10 km altitude range. Looking closely at Figure 6.1, a wave structure can be seen starting around 5 km and travels diagonally upward for an hour up to approximately 10 km. The image is too noisy to distinguish whether this wave is a gravity wave, but analysis of the data can inform one of the state of the system.

When looking at the amount of counts collected per altitude range, as depicted in Figure 6.2, one sees a large relative increase in counts around 2-8 km. This large lumped range of increase counts followed by a normal slow decrease in counts at higher altitudes suggests that the photomultiplier is not responding linearly at low altitudes. At altitudes higher than 8km, the slow constant drop in collected photon counts informs one that the system is functioning properly and can be related to the decrease in expected counts from the lidar forward model. Therefore it is nearly

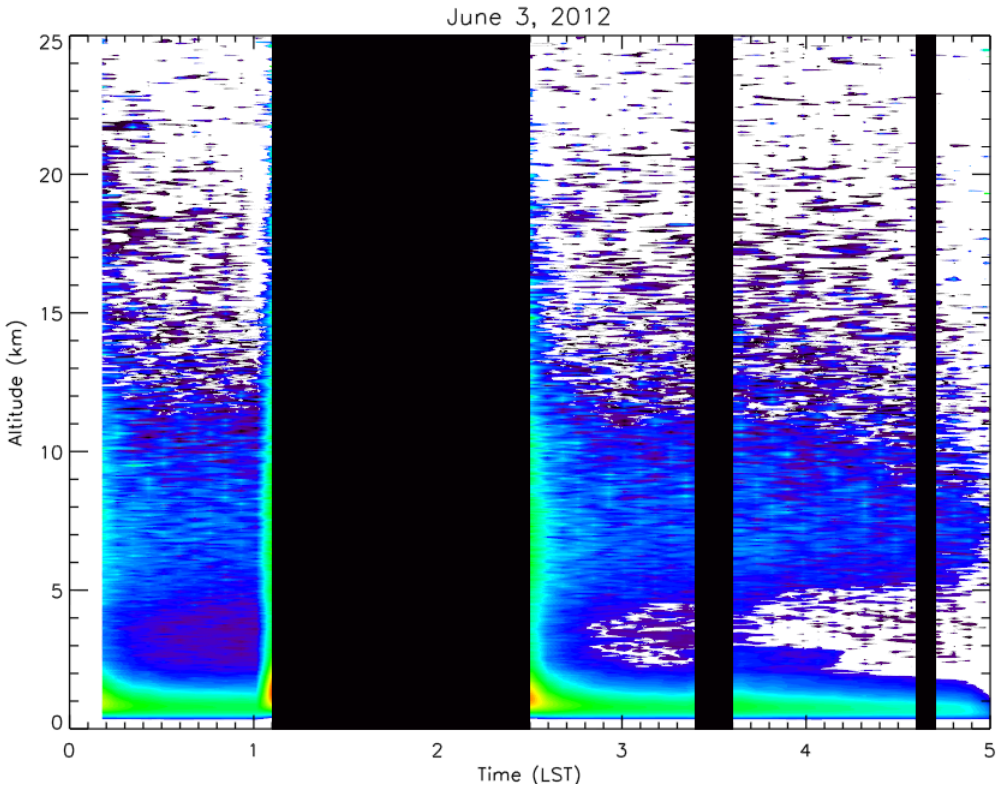

Figure 6.1 Data Taken on July 3rd 2012. Plot Produced by Andrew Gerrard.

certain that the photomultiplier tube is saturated by the flux of photons collected at low altitudes and functioning normally (and not saturated) starting at 8 km.

Assuming the PMT is saturated below 8km, analysis of the data at higher altitudes may produce desired results. Figure 6.3 shows the relative density perturbations above 8km for an hour of data collection at 5 minute time intervals.

This is done by first by calculating the density per altitude range ρ by using the equation:

$$\rho = (\sum_{i=0}^{9}(N_z - N_b)) \cdot z^2 \tag{6.1}$$

where N_z is the number of measured counts, N_b is the number of background counts, and z is the corresponding altitude range. The 10 term sum corresponds to the 10-30 seconds intervals that are added to obtain intervals of 5 minute intervals. Next an initial density ρ_0 is found by averaging the density per altitude of all the time

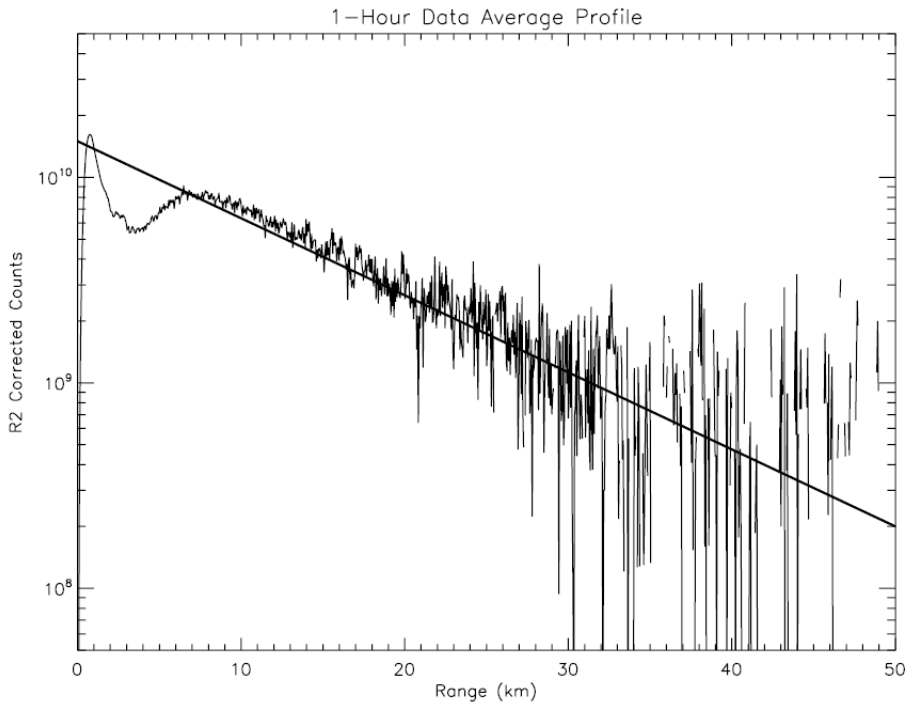

Figure 6.2 Total Return Counts Observed per Altitude Each Hour on July 3rd 2012. Plot Produced by Andrew Gerrard.

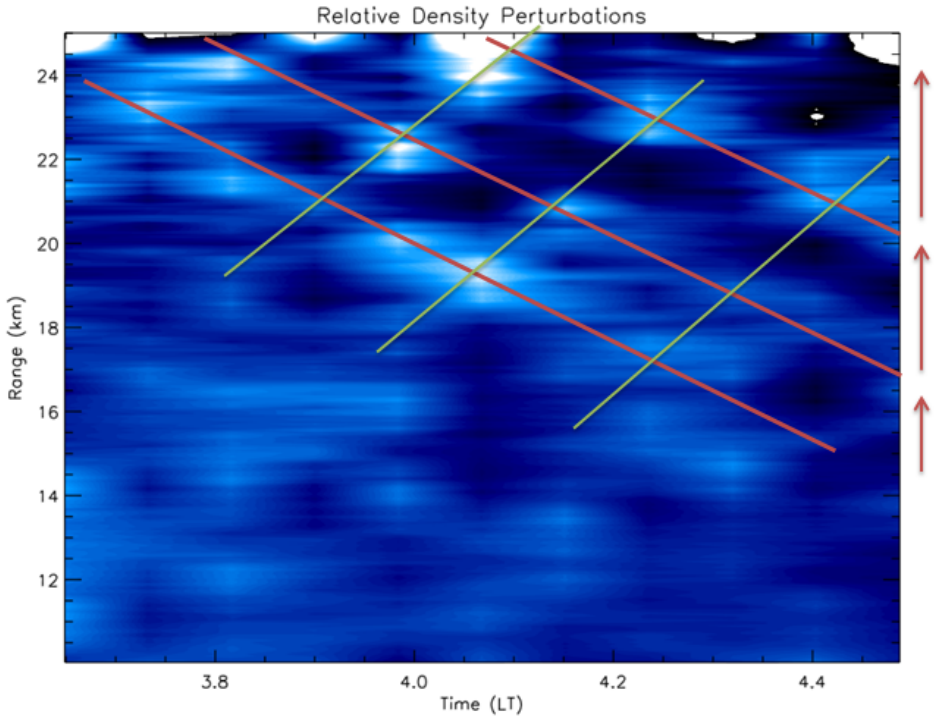

Figure 6.3 Wave Structure Observed on July 3rd 2012. Plot Produced by Andrew Gerrard.

intervals, i.e.:

$$\rho_0 = \frac{\sum_{i=0}^{N} \rho}{N+1} \tag{6.2}$$

where N is the number of time intervals in the data set. For Figure 6.3, $N = 12$ since each time interval is 5 minutes and the total data collection time was 1 hour. After the initial density is found, it can be subtracted to obtain a relative density ρ_r:

$$\rho_r = \frac{\rho - \rho_0}{\rho_0} \tag{6.3}$$

which is plotted per altitude, per time in the figure. Upon looking at the figure, wave phase lines can be seen diagonally traveling upward and to the right which are depicted in red. In addition, gravity wave phase lines can also be observed traveling downward and to the right, indicated by green lines. This wave activity is most likely generated from topological sources similar to those described in Figure 4.5. The downward traveling phase lines hint at reflections between the ground surface and a layer of the stratosphere. Since the PMT was saturated, no accurate conclusions can be made about the structure and characteristics of this wave activity. A solution to prevent photomultiplier tube saturation in future campaigns is to add a mechanical chopper to the system. The chopper would operate at 10Hz and would block enough light to prevent the photomultiplier from saturation. Although the data are too noisy for proper wave analysis, knowing the system should properly function with the addition of a mechanical chopper offers promising future campaigns for the tropospheric-stratospheric lidar.

APPENDIX

A.1 Terminology

Ablation- to remove or dissipate by melting, vaporization, erosion.

Aperture- The effective diameter of a lens or mirror

Clear Air Turbulence- turbulent movement of air masses in the absence of any visual cues such as clouds, and is caused when bodies of air moving at widely different speeds meet.

Eulerian Reference Frame- A reference frame that contains a stationary observer watching a fluid in motion.

F-Number- The ratio of the lens's focal length to the diameter of the entrance pupil.

Hydrostatic Approximation- The pressure at any point in the ocean (atmosphere) is due to the weight of the water (air) above it. When vertical accelerations are small compared to the gravitational acceleration, the hydrostatic approximation is valid.

Isothermal Atmosphere- An atmosphere that is in hydrostatic equilibrium and in which the temperature is constant.

Kelvin-Helmholtz Instability- Occurs when a velocity shear in present in a continuous fluid. A Kelvin-Helmholtz instability also occurs when two fluids are traveling at different speeds interact. A physical example is wind blowing over the surface of water, and the waves it produces.

Lagrangian Reference Frame- A reference frame that contains an observer who is following alongside a particular section of the fluid.

LASER- Light amplification by stimulated emission of radiation. A light amplifier usually used to produce monochromatic (one frequency) coherent radiation in the infrared, visible, and ultraviolet regions of the electromagnetic spectrum.

Mechanical Chopper- A device that periodically interrupts a light beam. Mechanical choppers usually consist of a spinning disc with a cavity that allows for light entry once every rotation.

Nanometer- 10^{-9} m

Oscillator- An electronic device that produces an alternating output of known frequency

Perturbation- A departure by a celestial body from the trajectory it would follow if it moved only under the influence of a single central force.

Photon- A particle with zero rest mass consisting of a quantum of electromagnetic radiation. Photons travel at the speed of light and are required to explain the photoelectric effect and other phenomena that require light to have particle character.

Rayleigh Scattering- The process in which electromagnetic radiation is deflected by particles in a matter through which it passes. In Rayleigh scattering there is a change in phase but no frequency change.

Remote Sensing- The gathering and recording of information that does not involve actual contact with the object or area under study.

Shear- A force that acts parallel to a plane rather than perpendicularly, as with a tensile or compressive force.

Stratification- to form or place in strata, or layers.

Wave Dispersion - Concept that waves of different wavelengths travel at different phase speeds.

*Many of the definitions above have been taken from the Oxford Dictionary of Physics.

A.2 Matlab Code

A.2.1 Lidar Forward Model and Field of View Code

```
%Lidar Equation
%Anthony Teti
%Last Modified July 7th 2012
%-----------------------------------------------------------------
clc
clear
close all


%-----------------------------------------------------------------
%This part of the program declares all the variables
%used in the lidar equation
%-----------------------------------------------------------------
n = .8*.8*.5*.15;
%lidar efficiency =
%Telescope*Lens*Filter*PMT Quantum Efficiency
Ta =  0.825;
%one-way transmittance of the lower atmosphere
%Andy said 40% for 355nm and 80-85% for 532nm
Pl = 4;                         %laser power (W)
t = 30;                         %integration time (s)
%usually =10s for calibration and =30s for data collection
h = 6.63*10.^-34;               %plank's constant
c = 3*10.^8;                    %speed of light (m)
lambda = 532*10.^-9;            %wavelength (m)
```

```
SigmaEff = (5.45*((550/532)^4)*10^-28)/10000;
%effective molecule backscatter cross section (cm^2)
% converted to (m^2)
Ns =[2.5*10.^19, 1.5*10.^19, 8.5*10.^18, 4.2*10.^18, 1.8*10.^18,
 8.3*10.^17, 3.7*10.^17 1.7*10.^17 7.7*10.^16 3.8*10.^16
2.0*10.^16 1.1*10.^16 5.7*10.^15 3.0*10.^15 1.5*10.^15 7.4*10.^14
3.4*10.^14 2.3*10.^14 1.1*10.^14 4.9*10.^13 2.2*10.^13]*1000000;
%molecule density at range z(cm^-3)    converted to (m^-3)
DeltaZ = 48;                  %receiver range bin length(m)
%usually =6 for calibration and =48 for data collection

r = [1000 5000 10000 15000 20000 25000 30000 35000 40000 45000 ...
...50000 55000 60000 65000 70000 75000 80000 85000 90000 95000 ...
100000];
%altitude (m)
Nb = 1;
%expected photoncount per range bin per pulse due to
% background noise and dark counts
%NOTE:Nb is determined from measurements
R = 10;                       %10 Hz (1/s)   %laser pulse rate
Ar = (pi*(.105/2)^2)-(pi*(.032/2)^2);
%receiving telescope aperture area (m^2)
%Ar = (pi*(1.22/2)^2);                    %For ITEK
konst = n*Ta^2*Pl*t*SigmaEff*DeltaZ*Ar/((4*pi)*(h*c/lambda));
%All the constants of the lidar equation
% ------------------------------------
```

```
for i = 1:21
    Nz(i) = konst*Ns(i)/r(i)^2 ;
    %expected number of return Photon counts
end
N = Nz + (Nb)     %Adds the measured background counts to
%the Total number of photon counts collected Nz
B = sum(Nz)

plot(r,N,'.')
title('')
xlabel('Altitude (km)')
ylabel('Return Counts')
title('')

lnN = log(N);
figure
interpolateAltitude = 1000:1000:100000;
interpolateCounts = interp1(r,lnN,interpolateAltitude);
linearizeReturncounts = exp(interpolateCounts);

plot(linearizeReturncounts,interpolateAltitude,'.')
xlabel('Return Counts (Nz)')
ylabel('Altitude (km)')
%interpolates the expected return counts so that values
%for every one km can be found instead of 5km
```

```
figure
plot(N,r/1000,'.')    %z/1000 converts altitude in m to km
title('')
xlabel('Return Counts')
ylabel('Altitude (km)')          %Needs to be converted to km

for i = 1:100
error(i) = (sqrt(linearizeReturncounts(i))/...
(linearizeReturncounts(i)-Nb))*100;
end

for i = 1:100
error2(i) = (sqrt((linearizeReturncounts(i)/4)*4.5)/...
...((linearizeReturncounts(i)/4)*4.5-Nb))*100; %4.5W Error Percent
end

for i = 1:100
error3(i) = (sqrt((linearizeReturncounts(i)/4)*3.5)/...
...((linearizeReturncounts(i)/4)*3.5-Nb))*100; %3.5W Error Percent
end

%
% for i = 1:100
%  error(i) = (sqrt(linearizeReturncounts(i))/...
%(linearizeReturncounts(i)-Nb))*100;
%  end
%
%  for i = 1:100
```

```
%  error2(i) = (sqrt((linearizeReturncounts(i)/2)*2.5)/...
%...((linearizeReturncounts(i)/2)*2.5-Nb))*100; %2.5W Error Percent
%  end
%
%  for i = 1:100
%  error3(i) = (sqrt((linearizeReturncounts(i)/2)*1.5)/...
%...((linearizeReturncounts(i)/2)*1.5-Nb))*100; %1.5W Error Percent
%  end

figure
plot(error2,interpolateAltitude,'r')
hold on
plot(error,interpolateAltitude,'g')
plot(error3,interpolateAltitude,'b')

title('')

% xlabel('Percent Error')
% ylabel('Altitude (km)')
% q = legend('4.5W','4W','3.5W');
% set(q,'Interpreter','none')
% hold off

xlabel('Percent Error')
ylabel('Altitude (km)')
q = legend('2.5W','2W','1.5W');
set(q,'Interpreter','none')
hold off
```

```
%-------------------------------------------------------------------
%Field of view calculation
%-------------------------------------------------------------------
%-------------------------------------------------------------------
d = 0.1016;
%diameter of the mirror (m)
f = 1.47;
%focal length of the telescope (m)
Fnumber = 14;
%F number of the Telescope
TelescopeFieldofView = atan((d/2)/f)
 %Angle in degrees

beam = .008*4;
 %beam diameter multiplied by the beam expander (4x)
beam2 = .008;
lambda = 532*10^-9;
%Wavelength of the laser
y = 1.22*lambda/beam;
 %Inner part of Diffraction equation
yy = 1.22*lambda/beam2;
thetalaserBeamExpander = (asind(y)/(2))
%Angle of Diffraction of the laser
thetalaser = (asind(yy)/(2))
x = -200:1:200;
%Horizontal Distance (m)
q = x*tand(90-TelescopeFieldofView)/1000;
```

```
%Calculates the Telescope FOV, altitude in km
z = x*tand(90-thetalaserBeamExpander)/1000;
%Calculates the laser beam divergence profile, altitude in km
z2 = x*tand(90-thetalaser)/1000;

%-----------------------------------------------------------------
%Plots the Field of view with the beam not being expanded
figure
plot(x,abs(q))
hold on
plot(x+1,abs(z2),'r')
%the x+1 takes into account the distance between the
%laser and telescope
hold off
title('Field of View of 4inch Mead Telescope')
xlabel('Horizontal Distance (m)')
ylabel('Altitude (km)')
Legend('Telescope Field Of View','Laser Beam')
%(...,'Location','SouthEast') places the Legend in the bottom
%right of the figure
axis([-40 40 0 50])
%axis([xmin(m) xmax(m) ymin(km) ymax(km)])
%-----------------------------------------------------------------

%-----------------------------------------------------------------
%Plots the Field of view with the beam being expanded
%expander
figure
```

```
plot(x,abs(q))
hold on
plot(x+1,abs(z),'r')
%the x+1 takes into account the distance between the
%laser and telescope
hold off
title('Field of View of 4inch Mead Telescope
using a 4x Laser Beam Expander')
xlabel('Horizontal Distance (m)')
ylabel('Altitude (km)')
Legend('Telescope Field Of View','Laser Beam')
%(...,'Location','SouthEast') places the Legend in the bottom
%right of the figure
axis([-40 40 0 50])
%axis([xmin(m) xmax(m) ymin(km) ymax(km)])

%-----------------------------------------------------------------
```

A.2.2 Data Analysis Code

```
%NJIT Lidar Data Analysis Program
%Anthony Teti
%Date Modified 4-19-2012
%-----------------------------------------------------------------
%-----------------------------------------------------------------
%-----------------------------------------------------------------
%THE ONLY PARAMETERS THAT NEED TO BE ADJUSTED IS THE BIN WIDTH (m)
%and the INTEGRATION TIME. ALL OTHER PARAMETERS ARE CALCULATED
%FOR YOU!!!
%-----------------------------------------------------------------
%-----------------------------------------------------------------
clear
close all
clc
binwidth = 48;                          %Receiver range bin width (m)
time = 30;                              %integration time in seconds

Data = importdata('C:\7-03-2012-0010.dat','\t');
%Specify the file name and path,
% this imports the data into an nxm array
[m,n] = size(Data);         %Determines the size of the nxm matrix

alt = ((1:n-1)*binwidth)/1000;
%Calculates the Altitude based on bin number and bin width
% and converts from m to km
```

```
integrationTime = (1:m)*time/60;

Timestamp = Data(1:m,1);
%grabs the first column of the data, which is the Time
% and constructs a 1xm matrix

TimestampString = num2str(Timestamp);
%Converts the Time numerical values into a String

A = TimestampString(:,1:2);
%Pulls out the year of the Timestamp
Century = '20';
Year = strcat(Century,A);
%Concatenates the string to create a 4 digit year

Month = TimestampString(:,3:4);              % 2 Digit Month
Day = TimestampString(:,5:6);                % 2 Digit Day
Hour = TimestampString(:,7:10);              % Military Hours

Data1 = Data(1:m,2:n);
 %The Lidar Data without the Timestamp
BackgroundRange = floor(sqrt(n));
%Finds the square root of n and rounds down to
% find how many bins will be considered background
minbin = n-BackgroundRange;
 %Finds the minimum background bin

for i = 1:m;
```

```
   Background(i) = mean(Data1(i,minbin:n-1));
%finds the average photon count in the "background"
%portion of the data

end
for i = 1:m;
    for j= 1:(n-1);
        Background1(i,j) = Background(i);
%Populates the 1xm matrix into an mxn matrix of background
    end
end

for i = 1:m;
    for j = 1:(n-1);
    Data2(i,j) = Data1(i,j)-Background1(i,j);
%constructs the new mxn matrix with the background subtracted
end
end

SumCountsPerBin = sum(Data2);
MeanCountsPerBin = sum(Data2)/m;
%Computes the average Photon counts per bin

MeanCountsPerInterval = sum(Data2')/m;
%Computes the average counts per interval
%Note that Data2' is the transpose of Data2
```

```
Concat1 = strcat(Hour(1,1),Hour(1,2));
Concat2 = strcat(Hour(1,3),Hour(1,4));
ConcatHour = strcat(Concat1,{':'},Concat2);

sumMeanCountsPerBin = sum(Data1);
%Sums the Raw data
figure                                    %Creates a figure window
plot(alt,sumMeanCountsPerBin)
mTextBox = uicontrol('style','text','position',[10 10 100 15]);
set(mTextBox,'String',strcat(strcat(Month(1,1),Month(1,2)),
{'/'},strcat(Day(1,1),Day(1,2)),{'/'},Century,
A(1,1:2),{' '},ConcatHour))
set(mTextBox,'Units','characters')
set(gcf,'Color',[1 1 1])
xlabel('Altitude (km)')
ylabel('Sum of Photon Counts')
title('Sum of Photon Counts Per Altitude (From Raw Data)')

figure
mTextBox = uicontrol('style','text','position',[10 10 100 15]);
set(mTextBox,'String',strcat(strcat(Month(1,1),Month(1,2)),
{'/'},strcat(Day(1,1),Day(1,2)),{'/'},Century,A(1,1:2),{' '},
ConcatHour))
set(mTextBox,'Units','characters')

%The next several lines of code make a few plots
%that will be displayed all in one figure window
subplot(3,1,1)
```

```
plot(alt,MeanCountsPerBin)
xlabel('Altitude (km)')
ylabel('Average Photon Counts')
title('Average Photon Counts Per Bin')
set(gcf,'Color',[1 1 1])

subplot(3,1,2)
plot(alt,log(MeanCountsPerBin))
xlabel('Altitude (km)')
ylabel('Log Average Photon Counts')
title('Log Average Photon Counts Per Bin')
set(gcf,'Color',[1 1 1])

subplot(3,1,3)
plot(integrationTime,MeanCountsPerInterval)
xlabel('Time (min)')
ylabel('Average Photon Counts')
title('Average Photon Counts Per Interval')
set(gcf,'Color',[1 1 1])

figure
plot(alt,MeanCountsPerBin)
mTextBox = uicontrol('style','text','position',[10 10 100 15]);
set(mTextBox,'String',strcat(strcat(Month(1,1),Month(1,2)),{'/'},
strcat(Day(1,1),Day(1,2)),{'/'},Century,A(1,1:2),{' '},
ConcatHour))
set(mTextBox,'Units','characters')
xlabel('Altitude (km)')
```

```
ylabel('Average Photon Counts')
title('Average Photon Counts Per Altitude')
set(gcf,'Color',[1 1 1])

figure
plot(alt,log(MeanCountsPerBin))
mTextBox = uicontrol('style','text','position',[10 10 100 15]);
set(mTextBox,'String',strcat(strcat(Month(1,1),Month(1,2)),{'/'},
strcat(Day(1,1),Day(1,2)),{'/'},Century,A(1,1:2),{' '},
ConcatHour))
set(mTextBox,'Units','characters')
xlabel('Altitude (km)')
ylabel('Log Average Photon Counts')
title('Log Average Photon Counts Per Altitude')
set(gcf,'Color',[1 1 1])



figure
imagesc(Data2');figure(gcf);
mTextBox = uicontrol('style','text','position',[10 10 100 15]);
set(mTextBox,'String',strcat(strcat(Month(1,1),Month(1,2)),{'/'}
,strcat(Day(1,1),Day(1,2)),{'/'},Century,A(1,1:2),{' '},
ConcatHour))
set(mTextBox,'Units','characters')
set(gca,'YDir','normal')
set(gca,'YTick',0:102:1024)
set(gca,'YTickLabel',{'0','5','10','15','20','25','30','35',
```

```
'40','45','50'})
set(gca,'XTick',0:20:120)
set(gca,'XTickLabel',{'0','10','20','30','40','50','60'})
set(gcf,'Color',[1 1 1])
xlabel('Time (min)')
ylabel('Altitude (km)')
title('')

figure
imagesc(Data2');figure(gcf);
mTextBox = uicontrol('style','text','position',[10 10 100 15]);
set(mTextBox,'String',strcat(strcat(Month(1,1),Month(1,2)),{'/'},
strcat(Day(1,1),Day(1,2)),{'/'},Century,A(1,1:2),{' '},
ConcatHour))
set(mTextBox,'Units','characters')
axis([0 120 0 312])
set(gca,'YDir','normal')
set(gca,'YTick',0:102:1024)
set(gca,'YTickLabel',{'0','5','10','15','20','25','30','35',
'40','45','50'})
set(gca,'XTick',0:20:120)
set(gca,'XTickLabel',{'0','10','20','30','40','50','60'})
set(gcf,'Color',[1 1 1])
xlabel('Time (min)')
ylabel('Altitude (km)')
title('')

figure
```

```
plot(alt,SumCountsPerBin)

%-----------------------------------------------------------------------
```

A.3 Construction Photos of the Jeffer Observatory

(a) (b)

Figure A.1 Preliminary Excavation of the Jeffer Observatory. Photos Taken By Diane and Gil Jeffer.

(a) (b)

Figure A.2 (a) Excavation of the Jeffer Observatory. (b) Quarry Process Added to Increase Future Foundation Strength. Photos Taken By Diane and Gil Jeffer.

(a)

(b)

Figure A.3 (a) Inner Forms Constructed. (b) Concrete Poured Into the Form to Make a Foundation. Photos Taken By Diane and Gil Jeffer.

(a)

(b)

Figure A.4 (a) Extreme Weather Halted Construction. (b) Outer Walls of the Foundation are Finished. Photos Taken By Gil Jeffer.

(a)

(b)

Figure A.5 (a) Area Surrounding the Foundation is Filled. (b) Quarry Process Filled and Compacted in Preparation for a Concrete Slab. Photos Taken By Gil Jeffer.

(a)

(b)

Figure A.6 (a) Concrete Slab Finished. Outlines are Made for the Construction of the Electronics Shed (b) Electronics Shed Built. Photos Taken By Diane and Gil Jeffer.

REFERENCES

Brasseur, G. and S. Solomon (1986), *Aeronomy of the Middle Atmosphere*, 2nd ed., D. Reidel Publishing Company, Boston, Massachusetts.

Coleman, T. (2008), Gravity Waves Make Tornadoes, *NASA Science*.

Collis, R. (1965), Lidar Observations of Clouds, *Science*, *149*, 978-981.

Daintith, J. (2009), *Oxford Dictionary of Physics*, 6th ed., Oxford University Press, New York, New York.

Division of Parks and Forestry (2012), *Jenny Jump State Forest*, New Jersey Department of Environmental Protection.

Driggers, R. G. (2003), *Encyclopedia of Optical Engineering*, vol. 3, Marcel Dekker, New York, New York.

Dutton, J. A. (1970), Clear Air Turbulence: A Mystery May Be Unfolding, *Science*, *167*.

Fritts, D. C., and M. J. Alexander (2003), Gravity Wave Dynamics and Effects in the Middle Atmosphere, *Reviews of Geophysics*, *41*, 1-124.

Gardner, C. S. (1989), Sodium Resonance Fluorescence Lidar Applications in Atmospheric Science and Astronomy, *IEEE*, *77*, 408-418.

Gill, A. E. (1982), *Atmosphere-Ocean Dynamics*, International Geophysical Series, vol. 30, Academic Press, San Diego, California.

Hecht, E. (2001), *Optics*, Addison Wesley, Reading, Massachusetts.

Hulburt, E. O. (1937), Observations of a Searchlight Beam to an Altitude of 28 Kilometers, *Journal of the Optical Society of America*, *27*, 377-382.

Koroshetz, J. E. (2005), Fiber Lasers for Lidar, *IEEE*.

Maiman, T. H. (1960), Stimulated Optical Radiation in Ruby, *Nature*, *187*.

McCann, D. W. (2001), Gravity Waves, Unbalanced Flow, and Aircraft Clear Air Turbulence, *MOAA/National Weather Service*, *25*.

Measures, R. M. (1984), *Laser Remote Sensing Fundamentals and Applications*, Kreiger Publishing Company, Malabar, Florida.

Nappo, C. J. (2002), *An Introduction to Atmospheric Gravity Waves*, International Geophysical Series, Academic Press, San Diego, California.

Parker, S. P. (1984), *McGraw-Hill Concise Encyclopedia of Science and Technology*, 1st ed., McGraw-Hill, New York, New York.

Products for Research Inc. (2012), *PC406CE Photomultiplier Tube Housing Specifications*, Danvers, Massachusetts.

Salby, M. L. (1996), *Fundamentals of Atmospheric Physics*, Academic Press, San Diego, California.

Speigel, E. A. and G. Veronis (1960), On the Boussinesq Approximation for a Compressible Fluid, *Astrophysical Journal*, *131*.

Stanford Research Systems (1990), *Model SR430 Multichannel Scaler/Averager*, Stanford Research Systems, Sunnyvale, California.

Taylor, N. (2000), *LASER: The Inventor, the Nobel Laureate, and Thirty-Year Patent War*, Simon and Schuster, New York, New York.

USGS (2012), The National Map Seamless Server Viewer.